



# RAM

● ROBOTICS  
AND  
MECHATRONICS

## 3D PRINTED CALORIMETRIC FLOW SENSOR

A. (Ameya) Umrani

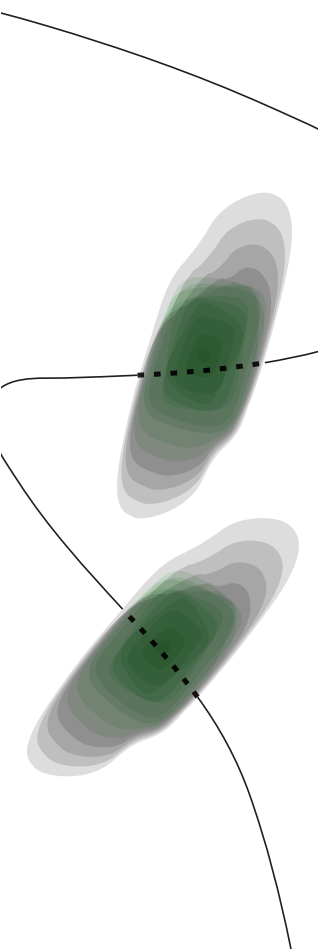
MSC ASSIGNMENT

**Committee:**

prof. dr. ir. G.J.M. Krijnen  
G.J.W. Wolterink, MSc  
dr. ir. E. Dertien  
dr. ir. R.J. Wiegerink

July, 2020

024RaM2020  
Robotics and Mechatronics  
EEMCS  
University of Twente  
P.O. Box 217  
7500 AE Enschede  
The Netherlands



## Summary

This study introduces a systematic approach towards modelling, designing and characterisation of a 3D printed flow sensor using thermal readout technique. Based on the principle of thermal flow sensing, a calorimetric flow sensor was fabricated using Fused deposition modelling. A model is presented based on the previous work done by Joël Van Tiem which predicts the heat distribution of a fluid in a channel with time independent and time dependent flow. The two sensors measure the temperature profile surrounding a heater and the resulting temperature change can be translated to flow in the channel.

The thermoresistive behaviour of the sensor material PI-eTPU 85 was also studied to determine the coefficient of thermal expansion of the material. The sensor material was placed in a regulated temperature chamber and subjected to heating and cooling cycles. Resistance was measured (per degree Celsius rise in temperature) using a four point measurement technique .

Two designs of the sensors are fabricated using fused deposition modelling 3D printer. An experimental setup has been designed to compare the model results with the experimental results.

## Acknowledgement

I would first like to acknowledge Prof. Gijs Krijnen for introducing me to the area of 3D printed sensors and its applications and giving me a nice opportunity to be a part of "Nifty group". I am truly grateful to you for guiding me throughout the entire thesis and making me dive deeper into the area of research. Next, I would like to thank my daily supervisor Gerjan Wolterink for giving valuable feedback on my work and helping me during experiments and 3D printing. The brainstorming sessions especially during the abstract writing were really nice. I would like to thank all my colleagues in Nifty group, Remco (Pino) for helping me during the measurements, Alexander for providing me quality research papers and Martijn for helping me in MATLAB scripts. Finally I also thank my parents for being strong and supportive throughout the thesis, your emotional support was truly valuable. Last but not the least I thank my wife for helping me in report writing and being a constant motivator.

# Contents

<b>1</b>	<b>Introduction</b>	<b>3</b>
1.1	Motivation . . . . .	3
1.2	Previous Work . . . . .	3
1.3	Context . . . . .	4
1.4	Project Goals . . . . .	4
1.5	Approach . . . . .	4
1.6	Report Structure . . . . .	5
<b>2</b>	<b>Thermal Modelling of Flow Sensor</b>	<b>6</b>
2.1	Introduction . . . . .	6
2.2	Study of types of Thermal Flow Sensors . . . . .	6
2.3	Previous Work . . . . .	7
2.4	Fluid Dynamics . . . . .	9
2.5	Thermal Equation . . . . .	10
2.6	Results . . . . .	15
2.7	Conclusion . . . . .	16
<b>3</b>	<b>Characterisation of Thermal properties of PI-eTPU 85-700+</b>	<b>17</b>
3.1	Related Work . . . . .	17
3.2	Experiments to study the thermoresistive properties of PI-eTPU 85-700+ . . . . .	17
3.3	Observations . . . . .	18
3.4	Discussion . . . . .	23
3.5	Conclusion . . . . .	23
<b>4</b>	<b>Fabrication</b>	<b>24</b>
4.1	Design . . . . .	24
4.2	Fabrication of Sensor . . . . .	24
<b>5</b>	<b>Experimental Methods</b>	<b>26</b>
5.1	Pressure driven flow . . . . .	26
5.2	Syringe pump setup . . . . .	27
5.3	Readout Design . . . . .	28
5.4	Signal Analysis . . . . .	29
5.5	Conclusion . . . . .	30
<b>6</b>	<b>Results and Discussion</b>	<b>31</b>
6.1	Pressure driven pump setup Measurements . . . . .	31
6.2	Syringe pump setup Measurements . . . . .	34

CONTENTS	5
<b>7 Conclusion</b>	<b>36</b>
<b>8 Future Work</b>	<b>37</b>
<b>A Appendix</b>	<b>38</b>
A.1 Constants derivation for time independent constant flow . . . . .	38
A.2 Effect Of Printing direction on the resistivity . . . . .	39
A.3 Abtract IEEE SENSORS . . . . .	39
<b>Bibliography</b>	<b>40</b>



## Nomenclature

$\alpha$	Temperature Coefficient of Resistance
$\delta t$	Time interval
$\delta t$	time of flight
$\delta x$	Displacement
$\rho$	Fluid Density
$A$	Surface Area
$c_p$	Specific heat capacity at constant pressure
$f$	Body force
$k$	Thermal conductivity
$L$	Channel half length
$n$	Thermal Diffusivity
$P$	Power in watts
$p$	Pressure
$Q$	Heat source density
$T$	Temperature
$T_{amb}$	Ambient temperature
$V$	Volume of fluid
$v$	Average fluid velocity

## List of Acronyms

**CB,CPC** - Carbon Black, Carbon Polymer Composites

**TPU** - Thermoplastic PolyUrethane

**CNT**- Carbon Nanotube

**TCR** - Thermal Coefficient of Resistance

**SEM** - Scanning Electron Microscope

**TEM** - Transmission Electron Microscope

**FDM** - Fused Deposition Modelling

**PTC** - Positive Temperature Coefficient

**NTC** - Negative Temperature Coefficient

**GUI** - Graphic User Interface

**CAD** - Computer Aided Design

# 1 Introduction

## 1.1 Motivation

Bio inspired sensors are upcoming in the field of sensor development. Stroble et.al [1] have provided an overview of wide range of biomimetic sensor technologies in their paper "An Overview of Biomimetic Sensor Technology". Research on Bio inspired 3D Printed sensors has been carried out by Professor Gijs Krijnen [2] at the Robotics and Mechatronics group which includes development of flow sensors being inspired by the sensing in cricket [3] and the whisker inspired tactile sensor [4] using 3D printing technologies. Likewise, the vestibular system in humans or in general in mammals can be mimicked partially, as it partially resembles the functioning of an angular acceleration sensor. The semicircular canals are rigid bony toruses in the inner ear filled with a fluid [5]. There are in total three semicircular canals mutually orthogonal to each other to sense the roll, pitch and yaw movement of the head as indicated in Figure 1.1. The deflections in the membrane caused by circular rotation of the head, induces stress in the hair cells (cilia) and a signal proportional to the rotation frequency is sent to the brain via the sensory nerve [6]. The current work focuses on how additive manufacturing can be used to print state of art angular acceleration sensors inspired by the human vestibular system design.

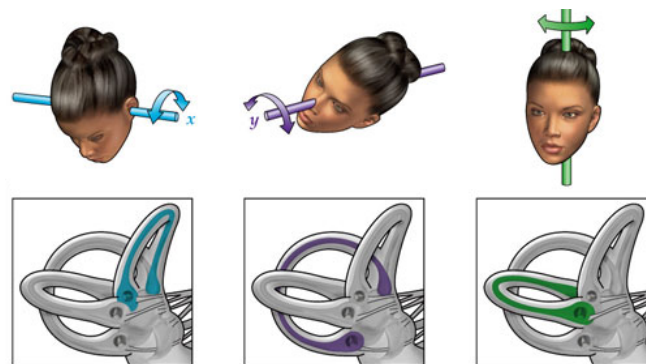


Figure 1.1: Movement of fluids in semicircular canal to head motion [7]

## 1.2 Previous Work

A lot of research has been carried out to mimic the functioning of the human vestibular system. Pierre Selva et. al. [8] developed a MATLAB simulink model to model the functioning of the human semicircular canals. A numerical model [9] describing the kinematics of the inner ear was described and simulated in MATLAB.

Alrowais et. al [10] designed a thermal angular accelerometer (using micro machined fabrication) mimicking the functioning of the human vestibular system using a thermal to electrical transduction mechanism. The sensor displayed a sensitivity of  $124\mu\text{V}/\text{deg}/\text{s}^2$ . Based on similar transduction principle and a lock-in amplifier to read the output from the sensors, a bio inspired angular acceleration sensor [11] was fabricated and characterised. One dimensional analytical model describing the heat transfer in the direction of the flow was modelled by Joël van Tiem for various flow conditions. The modelled results were then compared with numerical simulations using COMSOL.

A state of art 3D printed angular acceleration sensor was designed and characterised using electromagnetic readout technique by Joël et. al. [12].

### 1.3 Context

Recent advancement in the field of sensor development makes use of additive manufacturing for fabrication of sensors [13]. M.Schouten [14] demonstrated the use of commercially available materials for printing conductive structures using FDM. One such filament is a conductive Thermoplastic polyurethane (TPU) commercially known as PI-eTPU which will be used as a sensor material and a heater in this project. There are two variants of PI-eTPU commercially available, one with high resistivity of  $300 \Omega \text{ cm}$  available under the name of PI-eTPU 95-250 and other with a resistivity of  $80 \Omega \text{ cm}$  called as PI-eTPU 85-700+ which will be used in thesis. Sensors printed so far by 3D printing of PI-eTPU 85-700+ material include a flexible capacitive force sensor [15] [16], a tactile whisker sensor [4] and a compressive sensor used for measuring displacement [17]. First 3D printed version of EMG sensor using PI-eTPU 85-700+ was characterised by Gerjan et. al. [18] to sense muscle activity.

Printing factors such as temperature affect the performance of the sensor material as it also changes the electrical properties. By knowing the temperature dependence on the resistivity of these materials, it is possible to study the thermo resistive behaviour of the sensor. At the moment, very little information is available on how the effect of temperature causes the change in electrical properties of 3D printed carbon based filaments such as PI-eTPU 85-700+ which is one of the key findings of this research.

Due to time limitations it was not possible to model an angular acceleration sensor. A basic functioning and response of a flow sensor has been discussed in the subsequent chapters.

### 1.4 Project Goals

The main research question is "*Is it possible to manufacture a 3D printable flow sensor using FDM printing technology?*". The research focuses on studying the thermo-resistive behaviour of PI ETPU 85+ filament at different temperatures and printing conditions, developing an analytical model for estimating the behaviour of the sensor under flow and no flow conditions and choosing the appropriate sensor location for determining the maximum sensitivity and lastly perform experiments to validate the results. The following questions are addressed:

- How does the sensor material behave with changing temperature?
- Based on the thermal and electrical properties of the material, can it be used as a thermal sensor as well as a heater?
- What is the performance of the flow sensor?

### 1.5 Approach

The approach towards this research will be carried out using a scientific methodology which consist of three phases as listed below.

- **Phase I - Exploration Phase**  
The exploration phase consists of literature study to find out relevant scientific information on the research topic. Relevant models, theory behind the research questions, comparison of methods etc. will be studied during this phase.
- **Phase II - Modelling and simulation**  
Based on the literature review, an analytical model will be developed to model the system. The mathematical model will then be used to explore the sensor and systems behaviour using MATLAB.
- **Phase III - Experimentation and Verification**  
Experiments will be performed to study the thermoresistive behaviour of PI-eTPU 85

used in thermal sensing application. Once the sensor is 3D printed, it will be tested by inducing flow.

The sequence of steps followed to achieve the goals are as shown in below Figure 1.2.

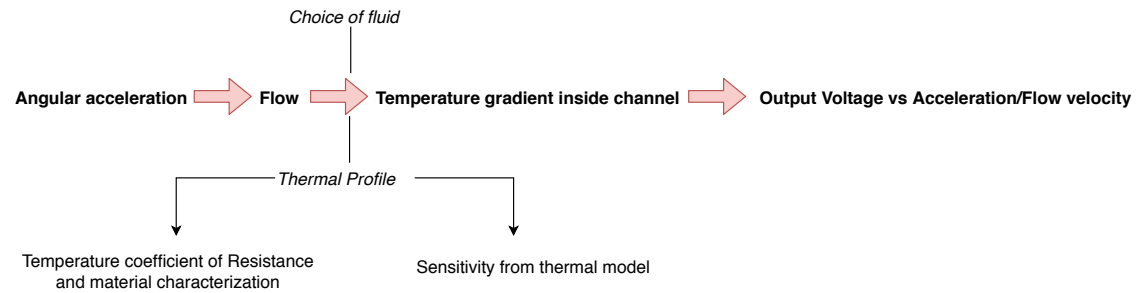


**Figure 1.2:** Flowchart of the workflow

## 1.6 Report Structure

Chapter 2 starts with discussion on different types of flow sensing techniques along with previous work done on thermal modelling of a calorimetric flow sensor. A new model based on changes in a previous model will be proposed along with results. Chapter 3 discusses the effect of temperature on the resistivity of PI-eTPU 85 samples and the effect of annealing. Furthermore, the effect of layer height, width and sample length on resistivity of samples is discussed. Chapter 4 consist of 3D printed sensor fabrication, flow driven setup and the readout method used in the experiments. Chapter 5 discusses measurements results from the flow experiments. The final Chapter 6 consists of overall conclusions and future scope.

## 2 Thermal Modelling of Flow Sensor

In this chapter various types of thermal flow sensors will be discussed and the choice of using calorimetric sensor will be motivated. In the second section different calorimetric flow sensors will be discussed along with previous work based on analytical modelling of calorimetric flow sensors. In the third section, the model developed by Joel van Tiem will be adapted for the current sensor design and finally the results will be evaluated for different conditions of flow, power and type of fluids.

### 2.1 Introduction

Before going to actual modelling of the sensor it is necessary to understand the principle of operation of the thermal flow sensor. The physics behind the operation of the thermal flow sensors can be traced back to 1914, when the Canadian physicist Louis Vessot King described the heat transfer in flow mathematically, [19] which later became famous as 'Kings Law'. Thermal flow sensors measure the flow rate of a liquid or gas by measuring the heat convected from a heated surface to the flowing fluid [20]. The thermal response to the flow is the change of the sensor's temperature which is measured electrically. The thermal sensors are isolated thermally so that the effecting heat transport in the fluid is dominantly by convection. There are various modes of thermal flow sensing namely, hot wire or anemometric sensors, calorimetric sensing and thermal time of flight sensing [21]. The principle used in the design of current sensor is calorimetric flow sensing, which will be explained later in the following chapter.

### 2.2 Study of types of Thermal Flow Sensors

Thermal flow sensors can be divided into three categories; Anemometric flow sensors, Thermal time of flight flow sensors and Calorimetric flow sensors. The principle of operation of all the three types of sensors is the same, a known quantity of heat is introduced into flowing stream of a liquid (or a gas) and measuring an associated temperature change. The components of a basic mass flow meter consist of two temperature sensors placed at a certain distance from the heater which is usually placed in the middle.

#### Anemometric Flow sensors

Anemometric flow sensors consist of a single heating element which also acts as a sensor. The heater element (which is kept at a temperature above the ambient temperature) is placed inside a flow channel and is heated by an electric signal. When flow is applied, the heat dissipated by the element is carried along in the direction of the fluid. The flow of fluid causes the heater element to cool down and the resistance to decrease. Hence, more power is required to maintain a constant temperature at the heater. The rate of cooling is proportional to the fluid velocity. Since the heater also acts as a sensor, the sensor element should be a resistor with high temperature coefficient  $\alpha$ . Anemometric sensors can be operated in one of three modes mentioned below [22].

- *Constant Power*: The resulting temperature of the resistor is used to calculate the fluid flow rate the higher the flow, the lower is the temperature of the resistive element
- *Constant Temperature*: The temperature of the heating element is maintained at a certain point above the ambient temperature and the power required to maintain that temperature is a measure of flow.
- *Temperature Balance*: In this method, the temperature difference between the sensor and the heater is kept constant by regulating the power to the heater [23].

### Thermal time of flight Flow sensor

The functioning of the thermal time of flight sensors is quite similar to the anemometric sensors except that instead of measuring temperature change, the time interval between application of heat pulse and arrival of the pulse at the sensor location is used to calculate the flow rate as below.

$$U = \frac{x}{\Delta t}$$

where  $U$  is the velocity of the fluid,  $x$  is the distance between heater and sensor and  $\Delta t$  is the time of flight of the pulse from heater to sensor. Note that this neglects the effects of thermal conduction in the fluid.

### Calorimetric Flow Sensing

The calorimetric flow sensing principle, finds applications in Micro flow sensing [24] [25] due to its suitability for small diameter tubing. Other advantages of using thermal sensors include broad dynamic range and high sensitivity [26]. In calorimetric flow sensing, two sensors and a heater are used. One sensor is placed in the upstream (before the heater element) and other in the downstream (after the heating element). Heating in the heater element by passing a current (joule heating) causes the fluid to increase temperature and store heat which subsequently is carried away by the fluid. The temperature sensors placed upstream and downstream, sense the temperature difference which is proportional to the input flow and hence is an indirect measurement of fluid velocity. The working of the calorimetric flow sensing is illustrated in the following figure 2.1.

Calorimetric sensors can again be subdivided into two types: non intrusive and intrusive anemometric sensors [24]. **Intrusive Type:** The sensors and heater are located inside the fluid. **Non-Intrusive type;** The heater and sensors are located on the outside of the tube surrounding the flow, flushing the channel.

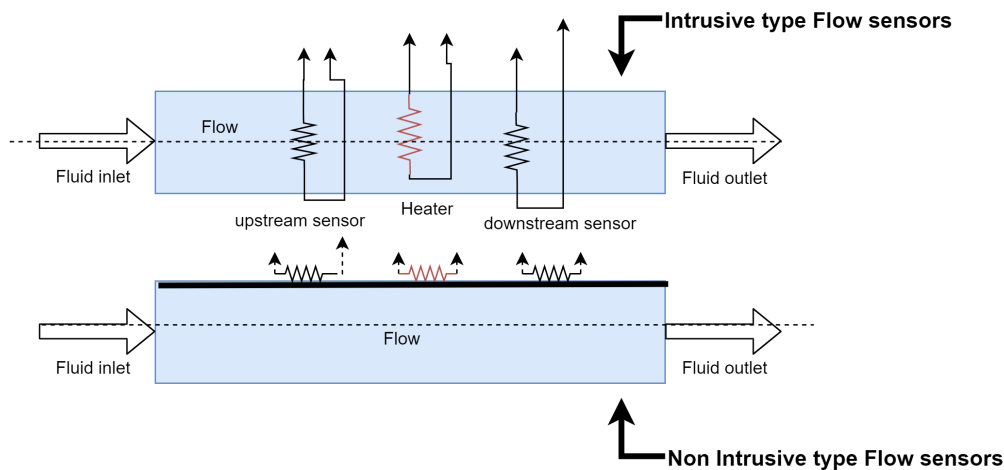
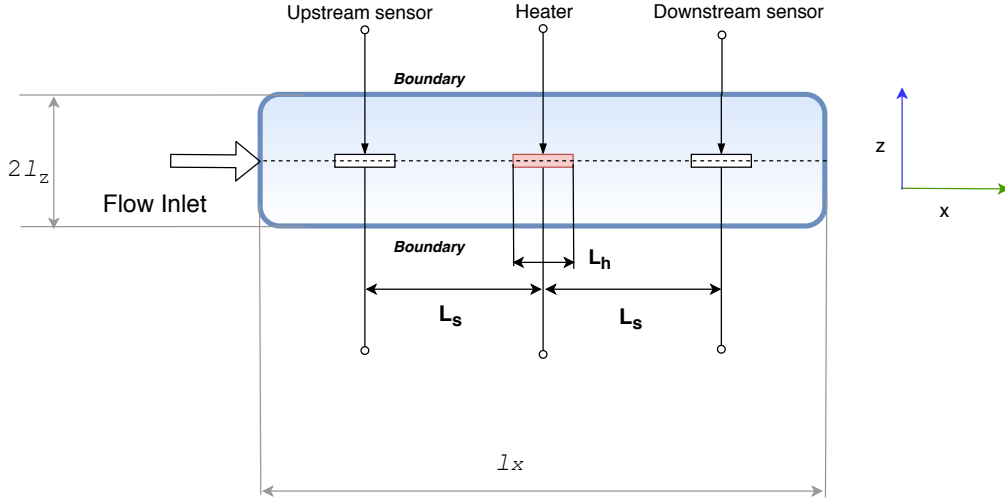


Figure 2.1: Intrusive and Non Intrusive type Calorimetric Sensor

### 2.3 Previous Work

Nam-Trung Nguyen [27] has developed analytical models for intrusive and non-intrusive calorimetric flow sensors. Since the sensor developed in this thesis is an intrusive type, the analytical model for intrusive type will be discussed in this section. Figure 2.2 represents the cut length section of the flow sensor,  $l_x$  is the total length of the sensor,  $2l_z$  is the total height of the sensor,  $l_h$  is the length of the heater element,  $l_s$  is the distance from heater to sensor assuming the left and right sensors are placed equidistantly from the heater element. The power

generated in the heater causes the heater to heat up, which also heats the surrounding fluid. The heat transport in the fluid occurs due to conduction and/or convection and is transported to the walls of the channel as represented in the Figure 2.2.



**Figure 2.2:** A typical calorimetric flow sensor [27]

The temperature distribution along the direction of flow can be modelled by using the heat balance equation of Temperature distribution ( $T$ ) with respect to the distance along the channel( $x$ ).

$$\frac{\partial^2 T}{\partial x^2} - \nu \left[ \frac{\rho c_p}{k} \right] \frac{\partial T}{\partial x} - \frac{T}{l_z^2} = 0 \quad (2.1)$$

$A = 2l_z \times l_y$ ,  $\rho$  is the fluid density,  $c_p$  is the specific heat capacity at constant pressure,  $\nu$  is the average fluid velocity and  $k$  is the thermal conductivity.

Let  $d = k/\rho c_p$  which is the thermal diffusivity of the fluid [28]. Solving the above differential equation with boundary condition  $\lim_{x \rightarrow \pm\infty} T(x) = 0$

$$T(x) = T_0 \exp \left[ \gamma_1 \left( x + \frac{l_h}{2} \right) \right] \quad \text{for} \quad \left( x < -\frac{l_h}{2} \right) \quad (2.2)$$

$$T(x) = T_0 \quad \text{for} \quad \left( \frac{l_h}{2} \leq x \leq \frac{l_h}{2} \right) \quad (2.3)$$

$$T(x) = T_0 \exp \left[ \gamma_2 \left( x - \frac{l_h}{2} \right) \right] \quad \text{for} \quad \left( x > \frac{l_h}{2} \right) \quad (2.4)$$

where

$$\gamma_{1,2} = \frac{\nu \pm \sqrt{\nu^2 + 2d^2/l_z^2}}{2d} \quad (2.5)$$

and

$$T_0 = \frac{P}{\left[ \frac{2kl_y l_h}{l_z} \right] + Ak(\gamma_1 - \gamma_2)} \quad (2.6)$$

The temperature difference between two sensors is found to be:

$$\Delta T(v) = T_0 \left[ \exp \gamma_2 \left( \frac{l_s - l_h}{2} \right) - \exp \gamma_1 \left( \frac{-l_s + l_h}{2} \right) \right] \quad (2.7)$$

A similar lumped model approach was used for the development of a Micro-liquid flow sensor by Lammerink et. al. [29]. Although the analytical model gave a fair estimation of the temperature distribution along the channel, the dynamics of the system were not well defined especially at the heater location. The eigen values (constants in the equation)  $\lambda_1, \lambda_2$  which depend on the flow velocity  $v$  need to be theoretically evaluated which makes the model more complex. The heat distribution along the heater length was assumed to be uniform and constant, which in real case is dynamic in nature. Moreover, the model holds true for relatively low flow velocities.

Considering the above limitations of the model, an analytical model developed by van Tiem et. al. [30] will be used in this thesis. The model by Joël incorporates more boundary conditions and can be used for relatively high flow velocities.

## 2.4 Fluid Dynamics

For, the sake of simplicity in the model, we assume zero flow and constant flow (velocity at given point is constant) conditions. The fluid flow in a channel can be related to a tubular laminar flow as shown in Figure 2.3(a). The profile of fluid flowing inside the channel is parabolic in shape, with different magnitudes at different points. The velocity is minimum at the edges while maximum at the centre of the tube as indicated in the Figure 2.3(b). Considering a volumetric flow:

$$\Lambda = \int_A \frac{\partial \vec{x}}{\partial t} \cdot d\vec{A} = \int_A \vec{v} \cdot d\vec{A} \approx \frac{V}{\Delta t} \approx A \frac{\Delta x}{\Delta t} \quad (2.8)$$

Here  $\Delta t$  is the time interval,  $\Delta x$  is the displacement of a given volume  $V$ , and the last approximations only hold for uniform velocity over the area  $A$ . For simplification, the average velocity (indicated by the vertical dotted line in Figure 2.3(b)) of the fluid is taken which is indicated by  $v_{\text{avg}} = \frac{\int v dA}{A}$ . The product of area times average velocity gives us the flow rate  $A v_{\text{avg}} = \int v dA$

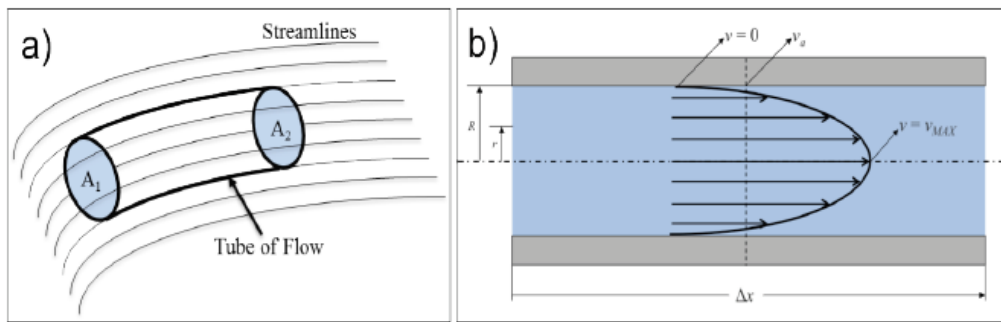


Figure 2.3: Flow velocity profile [31]

A more elaborate explanation of the velocity of the fluid inside the fluid channel can be expressed by Navier Stokes's Equation for incompressible flow.

$$\rho \left[ \frac{\partial \vec{v}}{\partial t} + \vec{v}(\nabla \cdot \vec{v}) \right] = -\nabla p + \mu \nabla^2 \vec{v} + \vec{f} \quad (2.9)$$

where  $\rho$  is the density of the liquid.  $\vec{v}$  is the fluid velocity,  $p$  is the pressure,  $\vec{f}$  is the forcing function (external forces acting on fluid body). The change in fluid velocity can then be modelled using Equation 2.10.

$$\frac{\partial \vec{v}}{\partial t} = -(\nabla \cdot \vec{v}) \vec{v} - \frac{1}{\rho} \nabla p + \frac{\mu}{\rho} (\nabla^2 \vec{v}) \quad (2.10)$$

## 2.5 Thermal Equation

The thermal modelling starts with the generalised one dimensional heat equation as mentioned in equation 2.11.

$$\rho c_p \left[ \frac{\partial T}{\partial t} + (\vec{v} \cdot \nabla) T \right] = k \nabla^2 T + Q \quad (2.11)$$

Where  $\rho$  is the fluid density,  $c_p$  is the specific heat capacity at constant pressure,  $T$  is the temperature,  $t$  is the time,  $v$  is the velocity,  $k$  is the thermal conductivity and  $Q$  is a heat source density.

### Case I: Zero Flow and time independent

Assuming zero flow through the channel, and temperature not time dependent. For modelling the sensor the geometry and boundary condition are defined. In the model there is one heater in the middle at  $x = \pm x_h$  and the ends of the sensor are located at  $x = \pm L$

$$k \nabla^2 T + Q = 0 \quad (2.12)$$

$$-k \frac{d^2 T}{dx^2} = \begin{cases} Q & \text{for } |x| \leq x_h \\ 0 & \text{Otherwise} \end{cases} \quad (2.13)$$

The above partial differential equation can be solved to obtain the temperature at three regions.

$$T(x) = \begin{cases} A_1 x + B_1 & \text{for } -L \leq x \leq -x_h \\ \frac{-Qx^2}{2k} + Cx + D & \text{for } |x| \leq x_h \\ A_2 x + B_2 & \text{for } x_h \leq x \leq L \end{cases} \quad (2.14)$$

To evaluate the 6 unknowns we need 6 equations which we will get from the various boundary conditions. We assume that the ends of the structure at  $x = \pm L$  are at room temperature  $T_{\text{amb}}$ :

$$T(-L) = T(L) = T_{\text{amb}} \quad (2.15)$$

At the heater region, the temperature should be continuous at  $x = \pm x_h$ :

$$T_{\text{left}}(-x_h) = T_{\text{heater}}(-x_h) \quad (2.16)$$

Similarly

$$T_{\text{right}}(x_h) = T_{\text{heater}}(x_h) \quad (2.17)$$

The heat flux should be continuous at  $x = \pm x_h$

$$\left[ k \frac{dT_{\text{left}}}{dx} \right]_{x=-x_h} = \left[ k \frac{dT_{\text{heater}}}{dx} \right]_{x=-x_h} \quad (2.18)$$

$$\left[ k \frac{dT_{\text{right}}}{dx} \right]_{x=x_h} = \left[ k \frac{dT_{\text{heater}}}{dx} \right]_{x=x_h} \quad (2.19)$$

Applying the above boundary conditions in equation 2.14 the 6 constants  $A_1, B_1, A_2, B_2, C, D$  can be evaluated.

$$A_1 = -A_2 = \frac{Qx_h}{k} \quad (2.20)$$

$$C = 0 \quad (2.21)$$

$$D = \frac{Qx_h(L - \frac{x_h}{2})}{k} + T_{\text{amb}} \quad (2.22)$$

$$B_1 = B_2 = T_{\text{amb}} + \frac{Qx_nL}{k} \quad (2.23)$$

### Case II: Time independent with constant flow

Now, introducing the effect of flow velocity, the heat equation becomes.

$$k \frac{d^2T}{dx^2} - \rho c_p v \frac{dT}{dx} = \begin{cases} Q & \text{for } |x| \leq x_h \\ 0 & \text{Otherwise} \end{cases} \quad (2.24)$$

The temperature along the flow can be calculated as follows:

$$T(x) = \begin{cases} A_1 e^{\frac{\rho c_p v x}{k}} + B_1 & \text{for } -L \leq x \leq -x_h \\ C_1 e^{\frac{\rho c_p v x}{k}} & \text{for } |x| \leq -x_h \\ A_2 e^{\frac{\rho c_p v x}{k}} + B_2 & \text{for } x_h \leq x \leq L \end{cases} \quad (2.25)$$

Substituting  $n = \frac{\rho c_p v}{k}$  and applying the boundary conditions of continuous temperature and heat-flow we have six equations as follows

$$\begin{aligned} A_1 e^{-nL} + B_1 &= T_{\text{amb}} & x = -L \\ A_1 e^{-nx_h} + B_1 &= C_1 e^{-nx_h} + C_2 - \frac{Qx_h}{nk} & x = -x_h \\ A_1 n e^{-nx_h} &= C_1 n e^{-nx_h} + \frac{Qx_h}{nk} & x = -x_h \\ A_2 e^{-nx_h} + B_2 &= C_1 e^{nx_h} + C_2 + \frac{Qx_h}{nk} & x = x_h \\ A_2 n e^{nx_h} &= C_1 n e^{nx_h} + \frac{Qx_h}{nk} & x = x_h \\ A_2 e^{nL} + B_2 &= T_{\text{amb}} & x = L \end{aligned} \quad (2.26)$$

After evaluation of constants the values of  $A_1, A_2, B_1, B_2, C_1, C_2$  are as follows: The derivation can be found in Appendix A.

$$\begin{aligned} A_1 &= \frac{Q(e^{n(L+x_h)} - e^{n(L-x_h)} - 2x_h n)}{n^2 k(e^{nL} - e^{-nL})} \\ A_2 &= \frac{Q(e^{-n(L-x_h)} - e^{-n(L+x_h)} - 2x_h n)}{n^2 k(e^{nL} - e^{-nL})} \\ B_1 &= -e^{-nL} \frac{Q(e^{n(L+x_h)} - e^{n(L-x_h)} - 2x_h n)}{n^2 k(e^{nL} - e^{-nL})} \\ B_2 &= -e^{nL} \frac{Q(e^{-n(L-x_h)} - e^{-n(L+x_h)} - 2x_h n)}{n^2 k(e^{nL} - e^{-nL})} \\ C_1 &= Q \frac{Q(e^{-n(L-x_h)} - e^{-n(L+x_h)} - 2x_h n)}{n^2 k(e^{nL} - e^{-nL})} \\ C_2 &= Q \frac{(1 + nx_h)e^{nL} - (1 + nx_h)e^{-nL} - e^{nx_h} + e^{-nx_h} + 2x_h n e^{-nL}}{r^2 k(e^{nL} - e^{-nL})} \end{aligned} \quad (2.27)$$

The parameters for simulation are indicated in Table 2.1 and 2.2.

**Table 2.1:** Geometry of proposed channel for simulation

Parameter	Value	Unit
Thickness of heater	10	mm
Width of Heater	10	mm
Length of Heater	3	mm
Diameter of channel	3	mm
Length of Channel	20	mm
Heater Power	0.5 - 1	W
Area of Channel	$5.7 \times 10^{-3}$	mm <sup>2</sup>
Area of heater	$21.20 \times 10^{-5}$	mm <sup>2</sup>

**Table 2.2:** Properties of material and fluids used in the simulation

Property	Value	Unit
Thermal conductivity of heater(TPU)	1.2	Wm <sup>-1</sup> K <sup>-1</sup>
Thermal conductivity of channel(semiflex)	0.2	Wm <sup>-1</sup> K <sup>-1</sup>
Thermal conductivity of deionised water	0.579	Wm <sup>-1</sup> K <sup>-1</sup>
Thermal conductivity of olive oil	0.17	Wm <sup>-1</sup> K <sup>-1</sup>
Density of olive oil	0.91	g cm <sup>-3</sup>
Density of deionised water	0.97	g cm <sup>-3</sup>
Heat capacity of deionised water	4.184	kJ kg <sup>-1</sup> K <sup>-1</sup>
Heat capacity of olive oil	1.97	kJ kg <sup>-1</sup> K <sup>-1</sup>

The effective conductivity of the sensor was calculated for the one dimensional model given by the equation below.

$$k_{\text{eff}} = \frac{k_{\text{heater}}A_{\text{heater}} + k_{\text{fluid}}A_{\text{fluid}}}{A_{\text{total}}} \quad (2.28)$$

It is assumed while developing the model that the effective heat transfer occurs to the fluid, losses to the surrounding were neglected.  $A_{\text{total}}$  is the cross sectional area. While deriving the analytical model the amount of heat generated by the heater was expressed as a heat source density and hence we require to divide the entire volume of the channel to get the effective heat density in the channel given by Equation 2.29

$$Q = \frac{P}{V} = \frac{P}{\pi r^2 h} \quad (2.29)$$

where, . The change in temperature ( $\Delta T = T - T_{\text{amb}}$ ) vs flow velocity (mm s<sup>-1</sup>) can be obtained by plugging the constants derived in equation 2.25.

### Case III: Time varying flow

Considering a harmonic flow given by  $v = v_0 \exp(j\omega t)$  the heat equation now becomes

$$\rho c_p \left[ \frac{\partial T(x, t)}{\partial t} + v_0 \exp(j\omega t) \frac{\partial T(x, t)}{\partial x} \right] = k \frac{\partial^2 T(x, t)}{\partial x^2} + Q(x) \quad (2.30)$$

Harmonic flow is considered because the flow in the channel is not constant in time. This is also the case when the direction of the sensor changes when the sensor is rotated even at constant velocity magnitude. The partial differential equation thus obtained has time dependent constants and therefore a closed form solution cannot be obtained. Considering conduction and convection process, the heat transfer due to conduction of a particle from the heater located at (x=0) to a sensor (x=L) is given by

$$t_{\text{cond}} = \frac{\rho c_p L^2}{k} \quad (2.31)$$

In case of convection the time needed is

$$t_{conv} = \frac{L}{v} \quad (2.32)$$

Considering the time required for heat conduction to be less than convection  $t_{cond} \ll t_{conv}$

$$\frac{\rho c_p L^2}{k} \ll \frac{L}{v} \quad (2.33)$$

or

$$v \ll \frac{k}{\rho c_p L} \quad (2.34)$$

As velocity is harmonic in time, addition of a small temperature  $\delta T$  is also harmonic. The total temperature is given by

$$\delta T_{tot}(x) = T(x) + \delta T_0(x) \exp(j \omega t) \quad (2.35)$$

Substituting above equation in equation 2.30 results into following expression

$$\rho c_p \left[ \frac{\partial T(x) + \delta T_0(x) \exp(j \omega t)}{\partial t} + v_0 \exp(j \omega t) \frac{\partial T(x) + \delta T_0(x) \exp(j \omega t)}{\partial x} \right] - k \frac{\partial^2 T(x) + \delta T_0(x) \exp(j \omega t)}{\partial x^2} = Q(x) \quad (2.36)$$

The term  $\rho c_p \left[ \frac{\partial T(x)}{\partial t} \right]$  can be neglected as it approximates to zero. The final expression becomes

$$\rho c_p \left[ \frac{\partial \delta T_0(x) \exp(j \omega t)}{\partial t} + v_0 \exp(j \omega t) \frac{\partial T(x) + \delta T_0(x) \exp(j \omega t)}{\partial x} \right] - k \frac{\partial^2 \delta T_0(x) \exp(j \omega t)}{\partial x^2} = Q(x) \quad (2.37)$$

Neglecting the smaller terms in the above equation we can obtain the following relation.

$$j \omega \delta T_0(x) - \frac{\partial^2 \delta T_0(x)}{\partial x^2} \frac{k}{\rho c_p} = \begin{cases} -v_0 \frac{Q}{k} x_h & \text{for } -L \leq x \leq -x_h \\ +v_0 \frac{Q}{k} x_h & \text{for } |x| \leq -x_h \\ +v_0 \frac{Q}{k} x_h & \text{for } x_h \leq x \leq L \end{cases} \quad (2.38)$$

Equation 2.38 consists of three second order non-homogeneous set of differential equations which can be solved using two sets of boundary conditions. Again, assuming temperature at the ends of the sensor to be equal to ambient temperature.

$$\delta T_0(-L) = \delta T_0(L) = 0 \quad (2.39)$$

The temperature and heat flux at the edge of the heater is given by.

$$\delta T_{0,\text{left}}(-x_h) = \delta T_{0,\text{heater}}(-x_h) \quad (2.40)$$

$$\delta T_{0,\text{right}}(x_h) = \delta T_{0,\text{heater}}(x_h) \quad (2.41)$$

$$\left[ k \frac{d\delta T_{0,\text{left}}}{dx} \right]_{x=-x_h} = \left[ k \frac{d\delta T_{0,\text{heater}}}{dx} \right]_{x=-x_h} \quad (2.42)$$

$$\left[ k \frac{d\delta T_{0,\text{right}}}{dx} \right]_{x=x_h} = \left[ k \frac{d\delta T_{0,\text{heater}}}{dx} \right]_{x=x_h} \quad (2.43)$$

Using above boundary conditions to solve equation 2.38 yields in the solution for  $\delta T_0(x)$

$$\delta T_0(x) = [A_i \text{re} + j A_i \text{im}] [\cos x(i) + j \cos x(i) \text{im}] - [B_i \text{re} + j B_i \text{im}] [\sin x(i) + j \sin x(i) \text{im}] \begin{cases} 1 & \text{for } -L \leq x \leq -x_h \\ -x/x_h & \text{for } |x| \leq -x_h \\ -1 & \text{for } x_h \leq x \leq L \end{cases} \quad (2.44)$$

The above expression is the representation of the change in temperature ( $\delta T$ ) as a function of space and time. The detail derivation of the constants are evaluated in the thesis of Joel van Tiem [30]. Considering only the amplitude modulus of the function.

$$|\delta T(x, t)| = |\delta T_0(x) \exp(j\omega t)| = |\delta T_0(x)| \quad (2.45)$$

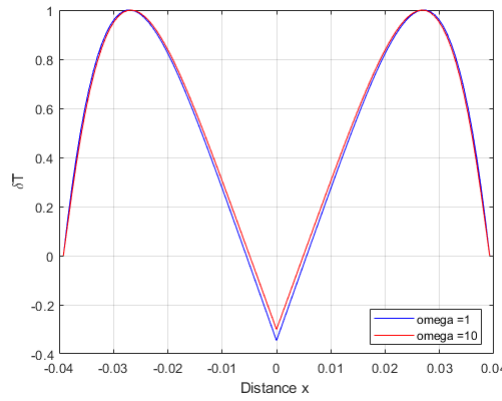


**Figure 2.4:**  $|\delta T_0(x)|$  for increasing value of  $\omega$

As seen in Fig 2.4  $|\delta T_0(x)|$  is symmetrical around  $x = 0$ . It can also be seen from the figure that the change in temperature is maximum at  $x = \pm L/2$ .

### Sensor positioning and sensitivity

The optimum position of placement of the sensor can be obtained by taking the second derivative of the temperature gradient  $\frac{dT}{dx}$ , which is also the condition of maxima. Hence

$$\frac{dT(x)}{dx} = \text{maximum} \quad \text{if} \quad \frac{d^2T(x)}{dx^2} = 0 \quad (2.46)$$

Substituting above condition in equation 2.25 of constant flow condition we get

$$x = \frac{1}{n} \ln \left[ \frac{\exp(nL)[\exp(nx_h) - \exp(-nx_h)]}{2x_h n} \right] \quad \text{for} \quad -L \leq x \leq -x_h$$

$$x = \frac{1}{n} \ln \left[ \frac{\exp(-nL)[\exp(nx_h) - \exp(-nx_h)]}{2x_h n} \right] \quad \text{for} \quad x_h \leq x \leq L \quad (2.47)$$

This is also the position where maximum sensitivity is obtained. Sensitive ( $S_v$ ) of the thermo resistive sensor is given by the ratio of sensor output ( $V$ ) and the flow rate ( $F$  i.e  $S_v = (\Delta V / \Delta F)$ )

## 2.6 Results

In this section the results of the simulation model developed earlier are presented. Non conductive fluids with high thermal capacity were chosen for the simulation, hence deionised water and olive oil were chosen. Different scenarios are presented as mentioned below. An increase in temperature led to an increase in resistance

- Constant power and changing flow velocity
- Constant velocity and changing heater power

### Simulation results for different flow velocities

Figure 2.5 shows the effect of changing the flow velocity on the thermal profile inside the fluidic channel for both distilled water and olive oil. Flow velocities are changed from  $0 \text{ mm s}^{-1}$  (no flow) to  $100 \text{ mm s}^{-1}$  (very high flow rates) assuming a constant power of  $300 \text{ mW}$  supplied to the heater.

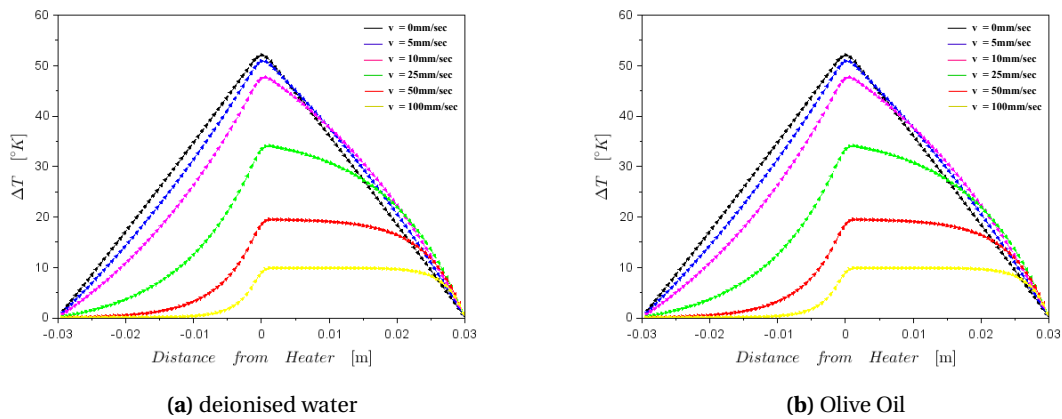


**Figure 2.5:** Change in temperature with respect to flow velocity  $P = 300 \text{ mW}$  (left) : deionised water . (right) : olive oil

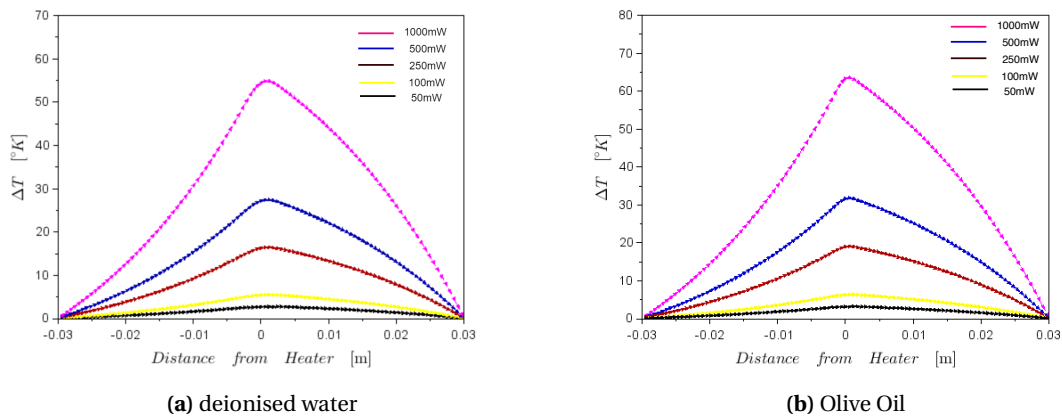


**Figure 2.6:** Effect of changing heater power on temperature distribution (left): deionised water . (right): olive oil at  $v = 10 \text{ mm s}^{-1}$ .

### **Effect Of Changing heater Power**

Figure 2.6 shows the effect of changing the heater power on the temperature distribution inside the channel for both olive oil and water. The heater power is increased from 50 mW to 1 W in steps keeping the flow constant at  $100 \text{ mm s}^{-1}$ .

### **2.7 Conclusion**

The more heat is generated in the channel, the higher is the temperature rise generated in the channel. When flow is induced, the heat is carried away from the heater in the direction of the flow and the heater cools down proportional to the flow rate. The thermal gradient causes the upstream temperature to rise and the downstream temperature to fall. For identical volume and constant flow, it is observed in Fig 2.6 that, the rise in temperature is higher for olive oil compared to deionised water due to the fact that the heat capacity of oil is much lower than that of water, making it easier for rapid heating and cooling applications. For higher heat capacity of fluid the RC time constant is less and higher is the bandwidth of the system. Evaluating the analytical results for sensor positioning, it is ideal to place the sensors equidistant to the heater.

---

## 3 Characterisation of Thermal properties of PI-eTPU 85-700+

The aim of this chapter is to select a study the temperature dependent electrical properties of carbon infused TPU for thermal sensing applications. As the sensor will be used as a thermistor, the thermo-resistance effect of the material will be studied.

### 3.1 Related Work

Although little research has been conducted on the thermoresistive properties of commercially available PI-eTPU 85 carbon infused TPU, Kiraly et. al [32] was the first to study the effect of polymer composites doped with carbon black. In his experiments it was observed that the specific resistivity increased as a function of temperature. Thermal and electrical properties of these materials were dependent on the filler concentration as observed by Ivanov et.al. [33]. The advantages of these materials are they are cheap, light in weight, and hence easy to 3D print with the help of conventional FDM 3D Printers [34].

### 3.2 Experiments to study the thermoresistive properties of PI-eTPU 85-700+

#### Aim

The aim of the experiment is to study the thermo-resistive properties of PI-eTPU 85 with the help of Resistance-Temperature (R-T) curves.

#### Objectives

Following effects will be studied while performing the experiments.

- Study of thermo-resistive behaviour.
- Comparison of 3D printed and normal filament of PI-eTPU of the same length.
- **Hysteresis** in 3D printed and filament samples.
- Temperature Co-efficient of Resistance(TCR)
- **Annealing effect** observed in PI-eTPU 85

#### Experimental Setup

In the initial phase a very basic setup was formed see Figure 3.1a, which consisted of an oven for heating the sample of a 5 cm long filament of PI- eTPU 85 with diameter of 1.75 mm, a thermocouple for measuring the temperature of the sample and a source measuring unit (*Keithley 6430*) for measuring the resistance. A conductive silver paint (width 2 mm, length 3 mm) was applied to the contacts in order to provide better electrical connectivity and also to minimise the contact resistance between the probe and sample. The ink was left to dry for about 15 min and then copper tape was connected to the sample for soldering the wires.

In order to reduce the measurement time, a better setup was developed as shown in Figure 3.1b in order to reduce the human errors in measurements and also save time. A data acquisition unit (make Agilent 34970A series) was introduced to measure the change in resistance along with a programmable oven to set temperatures. A GUI in labview was used to monitor the temperature change in resistance with respect to time. With the help of the GUI and a labview program it was possible to set the temperature profile (ramp up/ramp down cycles) for evaluating the hysteresis effects on the sample, which will be discussed in the results section. Moreover, it was possible to take measurements of more than one samples using a GPIO expansion board.

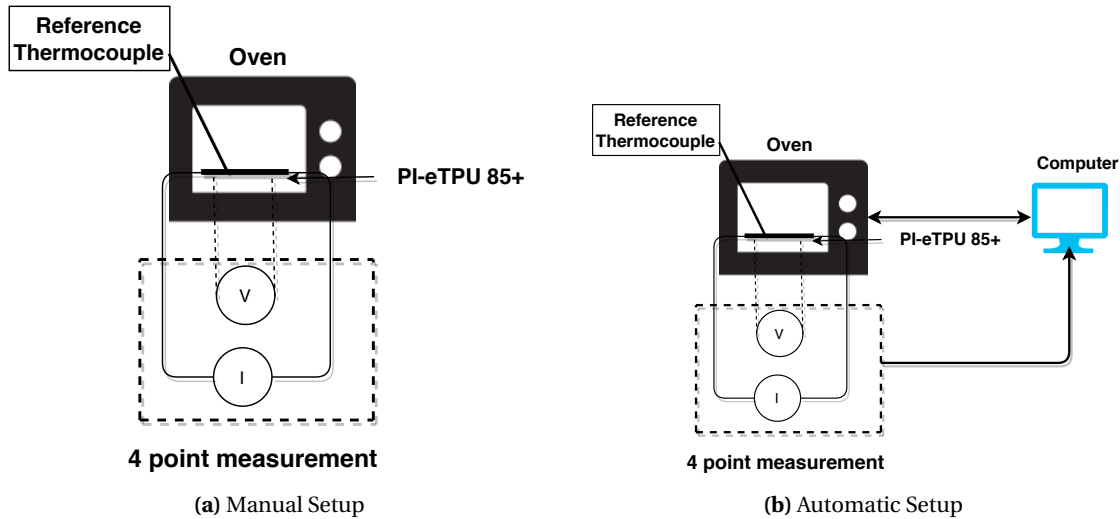


Figure 3.1: Experimental Setup

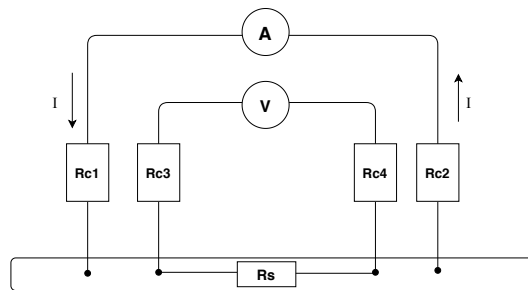


Figure 3.2: 4-point measurement performed on the sample.  $R_s$  represents the effective resistance

## Connections

A four point measurement technique is implemented while measuring the resistance of the wire as seen in Figure 3.2. Current  $I$  passing through the wire causes a potential ( $V_s$ ) to develop across the terminals of the sample, which is then sensed via the sensing terminal.  $R_{c1}$  and  $R_{c2}$  represent the contact resistance of the current leads and  $R_{c3}$  and  $R_{c4}$  represent the contact resistances of voltage sensing terminals. The 4-point measurement is preferred over the 2 point measurement as it eliminates the lead and contact resistance from the measurement [35] and the true resistance of the sample under test  $R_s$  is measured.

## 3.3 Observations

### 3.3.1 Thermo-resistive effects

#### Methods

The filament was baked in the oven at a maximum of  $160^\circ\text{C}$  and the change in resistance was noted down (manually) for each interval of  $5^\circ\text{C}$ . Figure 3.3 shows the thermo-resistive behaviour of PI-eTPU filament of length 7 cm.

#### Results

As seen in the figure 3.3 the resistance increases from  $19\text{ k}\Omega$  to  $160\text{ k}\Omega$  with an increase in temperature from  $23^\circ\text{C}$  to  $130^\circ\text{C}$  displaying the Positive temperature coefficient (PTC) effect. A sharp transition is observed at  $80^\circ\text{C}$  where the resistance rapidly starts increasing till  $130^\circ\text{C}$ . After reaching  $130^\circ\text{C}$  the resistance is seen to decrease from  $160\text{ k}\Omega$  to  $70\text{ k}\Omega$  even with an increase in temperature (NTC effect).

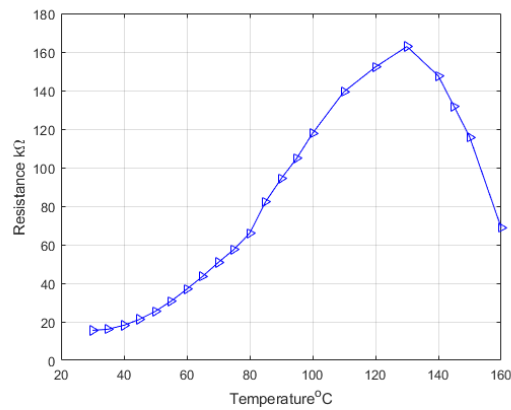
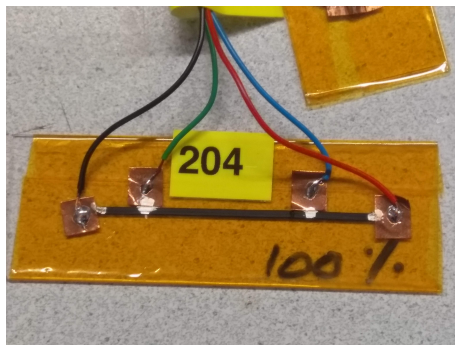


**Figure 3.3:** Sample of PI-eTPU filament displaying thermoresistive behaviour

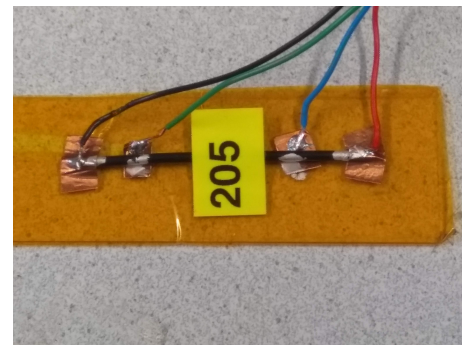
### 3.3.2 Comparison Between 3D printed vs Plain Filament of eTPU-85

#### Methods

The idea of the experiment was to compare the resistance of the 3D printed sample (Fig 3.4a) and a plain filament (Fig 3.4b) of same lengths. Both the 3D printed and the plain filament were placed in the oven at room temperature (24 °C). This time using the automatic setup as seen Fig 3.2, the resistances of the samples were monitored with respect to the temperature. Change of resistance was noted from 30 °C to 70 °C with an interval of 5 °C.



(a) 3D printed PI-eTPU 85 (l=5cm)



(b) Filament of PI-eTPU 85 (l=5cm)

**Figure 3.4:** Test samples for determining the thermoresistive effects

Sensor shape and dimensions(L x W)	Rectangular(50 mm x (0.5 mm)
Printing Temperature(°C)	210
Heat Bed Temperature (°C)	50
Infill Percentage	100
Extrusion Multiplier	1.25
Extrusion width (mm)	0.7
Printing speed(mm min <sup>-1</sup> )	2000
Nozzle diameter(mm)	0.8

**Table 3.1:** Used Printer settings for PI-ETPU 85-700+

## Results

It can be seen from the Figure 3.5 that the resistance of a 3D printed filament is a factor of 8 more than the resistance of an unprinted filament. A sharp decline in resistance is observed in the filament reading around 46 °C which might be due to a contact problem or due to manual errors while taking the measurement readings. In Figure 3.5 the blue markers indicate the resistance of 3D printed filament and the orange markers indicate the resistance of a plain filament. The left y - axis indicates the resistance of the 3D printed sample, right y - axis indicates the resistance of filament.

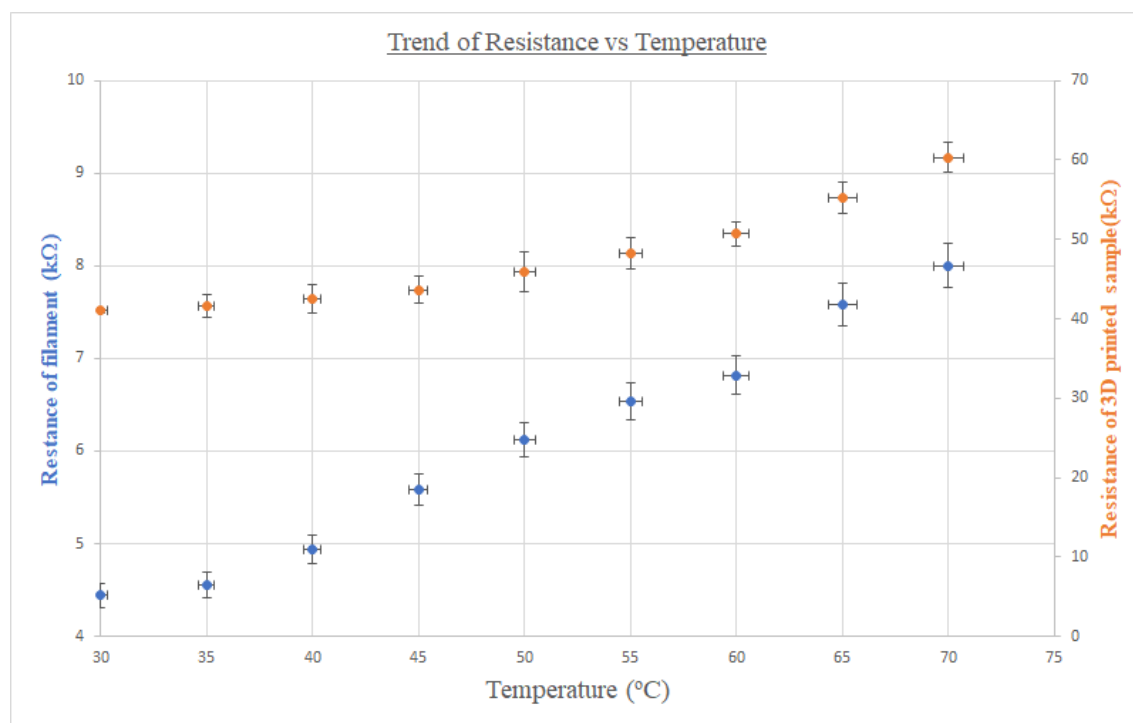


**Figure 3.5:** Resistance vs Temperature Trend in 3D printed (blue) vs plain filament of PI-eTPU 85 (orange)

### 3.3.3 Temperature Coefficient of Resistance of eTPU

Figure ?? shows the plot of the change in resistance  $(R - R_{ref})/R_{ref}$  against the change in temperature  $(T - T_{ref})$  as taken from the previous readings of Figure 3.5. The slope of the graph determines the temperature coefficient of resistance ( $\alpha$ ) for the ramp up cycle. The thermal coefficient of resistance, TCR, can be calculated using Equation 3.2, where  $R_0$  is the resistance measured at room temperature  $T_0$ .

$$\text{TCR} = \frac{dR}{dT \times R} = \frac{R - R_0}{(T - T_0) \times R_0}$$

$$R(T - T_0) = R_0 e^{\alpha(T - T_0)} \quad (3.1)$$

with  $R_0 = R(T_0)$  and  $\alpha > 0$  for PTC and  $\alpha < 0$  for NTC behaviour, and for which the Taylor expansion for small temperature variations becomes:

$$R(T - T_0) = R_0 \cdot [1 + \alpha(T - T_0)] \quad (3.2)$$

Calculating the average coefficient of resistance of 3D printed sample from Equation 3.1, was found to be  $0.0167 \text{ } ^\circ\text{C}^{-1}$  while that of the raw filament was found to be  $0.0232 \text{ } ^\circ\text{C}^{-1}$ . The resistivity of the 3D printed sample was found to be greater than that of a plain sample of eTPU. The sensitivity of material is directly proportional to the TCR of material [36].

### 3.3.4 Hysteresis Effect

#### Methods

For determining the hysteresis effect, a ramp up and ramp down temperature profile was selected. A sample of PI-eTPU 10 cm long was placed in the oven at room temperature. Change in resistance was noted from 40 °C to 120 °C with ramp up, and ramp down till 50 °C. After reaching the set temperature, the 10 cm long sample is cooled down to 50 °C.

#### Results

The following Figure 3.6 shows the change in resistance with respect to temperature. A PTC effect was observed till 110 °C after which the NTC effect crept in till 120 °C. As seen in the Figure 3.6, the sample showed an exponentially increasing trend of resistance with respect to temperature from 40 °C to 110 °C. The cooling cycle shows a decrease in resistance with noticeable hysteresis. Figure 3.7 shows the variation of TCR during ramp up and ramp down cycle. The TCR displays an exponential rise from  $0.002\text{ }^{\circ}\text{C}^{-1}$  till a maximum of  $0.024\text{ }^{\circ}\text{C}^{-1}$  at 110 °C as seen in Fig 3.7. This shows that the maximum TCR occurs at glass transition temperature.

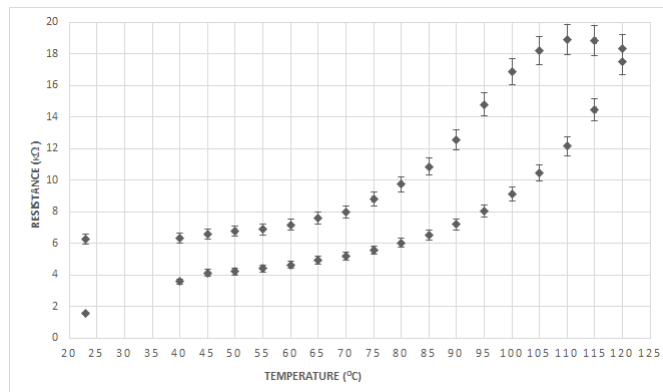


**Figure 3.6:** Resistance vs Temperature characteristic of 3D printed PI-eTPU 85

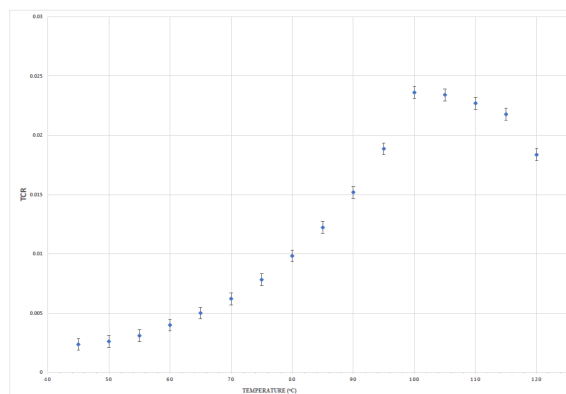


**Figure 3.7:** TCR from hysteresis experiment

### Annealing Effect

#### Methods

The effect of heating and cooling cycles(thermal stress)on the behaviour of 3D printed as well as plain filament of PI-eTPU 85 was studied. For this, the new setup was used in which the samples were gradually heated from 30 °C to 70 °C and cooled down in similar way with a temperature step of 6 °C. The experiment was repeated for four thermocycles and the change in

resistance was noted. There was a 6 hour long break before the second cycle started and the samples were allowed to cool down to room temperature.

## Results

Figure 3.8 shows the R-T curves for 4 cycles. The idea behind the experiment was to see if the values of resistance first observed in Figure 3.8a could be traced back. The cycles represent the number of temperature sweeps. From the above plots it can be seen that hysteresis effect is

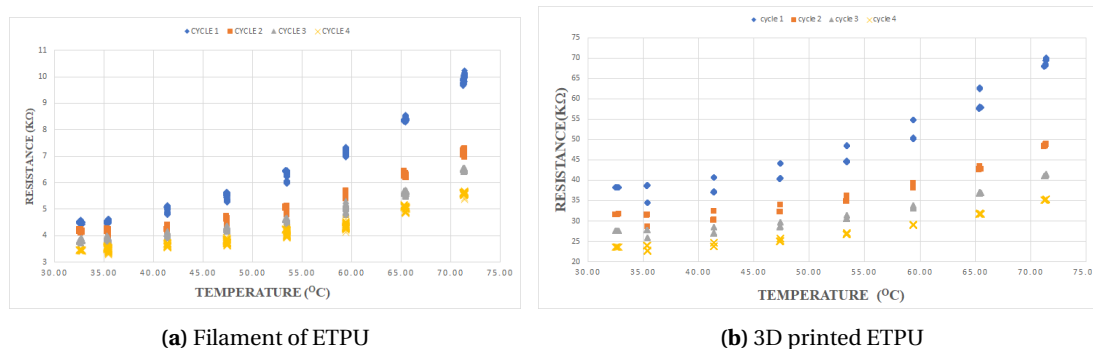


**Figure 3.8:** Temperature dependent Resistance behaviour of 3D printed filament and plain filament of length 5 cm

prominently observed in the R-T curves of 3D printed sample. Some hysteresis can be seen in the plain filament but not that prominent. Tables 3.2 and 3.3 indicate the percentage change in resistance between different cycles at 30 °C for both 3D printed and plain filament.

**Table 3.2:** Percent decrease Resistance at 30 °C for printed PI- eTPU 85-700+

Cycles	Initial Resistance kΩ	Initial Resistance kΩ	Change in Resistance
Cycle 1-2	38.26	31.47	17.74%
Cycle 2-3	31.47	27.72	11.91%
Cycle 3-4	27.72	24.04	13.27%
Cycle 1-4	38.26	24.04	37.16%

Comparing results from from the tables,it can be seen that the percent decrease in resistance in the plain filament is quite uniform whereas its irregular in case of 3D printing filament.Also, per cycle decrease in resistance, and hence the resistivity is more in 3D printed filament than the plain filament. Thus, the annealing effect affects the resistivity of PI-eTPU85,however, the temperature coefficient of resistance is retained and hence can be used for temperature sensitive applications.

**Table 3.3:** Percent Decrease in Resistance at 30 °C of PI-eTPU raw filament

Cycles	Initial Resistance kΩ	Initial Resistance kΩ	Change in Resistance
Cycle 1-2	4.46	4.127	7.46%
Cycle 2-3	4.127	3.81	7.68%
Cycle 3-4	3.81	3.498	8.18%
Cycle 1-4	4.46	3.498	10.76%

### 3.4 Discussion

The point at which the resistance no longer increases with increase in temperature is termed as the phase transition temperature of the material which is 130 °C as seen in Figure 3.3. Phase transition temperature is the temperature at which the phase of the material changes, for example from solid phase to liquid phase due to prolonged heating. In the case of thermo plastic polyurethanes, because of the prolonged heating at high temperature, gradual melting of the filament occurs and the material goes into a plastic zone from where it cannot be recovered anymore [37]. In some literature [38] this temperature is mentioned as glass transition temperature, but after carefully going through the literature [39] it was found that the glass transition temperature of TPU is below zero degrees and hence phase transition temperature.

An abrupt change in electrical resistivity was seen at the phase transition temperature at which the highest thermal expansion coefficient ( $\alpha$ ) was observed. Similar observations were made in the work by Aneli. et. al [40] and Hao et. al [41] in which the reason for PTC behaviour was studied. Based on their experiments and analysis it was believed that the PTC effect was due to the expansion between matrix and carbon black filler, whereas the NTC effect was assumed to be because of the formation of conducting networks at high temperature as explained by Klason et. al. [42]. At higher temperatures, the elastic modulus of the polymer matrix decreases leading to re-connection of the conductive pathways of the filler matrix [13]. Dominant NTC behaviour was observed in the work by Fraser et. al [43] in which the matrix was Poly-lactic acid and the filler content was carbon black and graphene.

An ideal temperature sensor should have minimum hysteresis, also termed as memory effect, when it is exposed to a sequential range of temperatures. The larger the hysteresis, the lesser is the repeatability observed in the sensor readings and the sensor needs to be re-calibrated after every experiment.

A high TCR is desired for good sensor material, the TCR of PI-eTPU 85 being almost a factor of 5 more than the TCR of Tungsten filament ( $0.0045 \text{ }^\circ\text{C}^{-1}$ ) it can be suitable in building temperature sensors.

### 3.5 Conclusion

Resistance-Temperature curves display both PTC and NTC effect after a phase transition temperature. A phase transition temperature of 130 °C was observed in plain filament and at 110 °C in 3D printed samples of PI-eTPU 85. It can be concluded from the observations that the sensor can be operated in the linear region between 25 °C to 70 °C where the rise in resistance with an increase in temperature is quite uniform. High TCR  $0.024 \text{ }^\circ\text{C}^{-1}$  observed in 3D printed samples, which is desirable in developing temperature sensors. Prolonged heating of the filament causes the resistance of PI-eTPU 85 to decrease, which is observed during its annealing.

## 4 Fabrication

This Chapter focuses on the materials used for printing the sensor, the print parameters, sensor design and a proof of concept setup along with the readout technique used.

### 4.1 Design

Two sensor designs were fabricated and tested as seen in Fig 4.1a and Fig 4.1b. To keep the design as simple as possible a rectangular geometry is introduced. Heater is located at the centre of the channel and the two sensors are placed symmetrically with respect to the heater location.

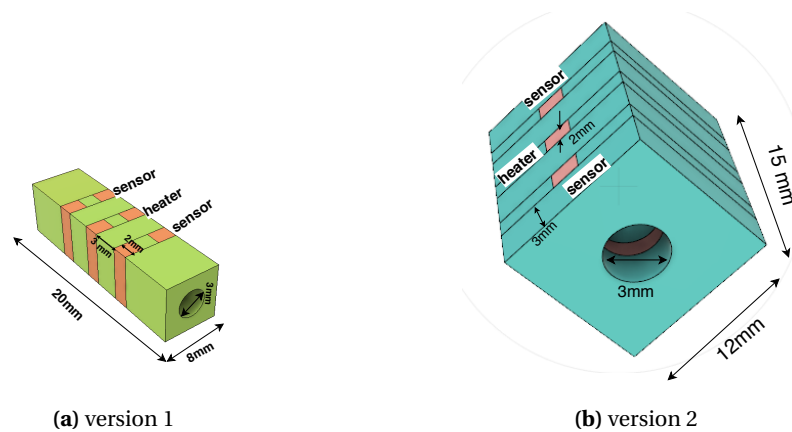
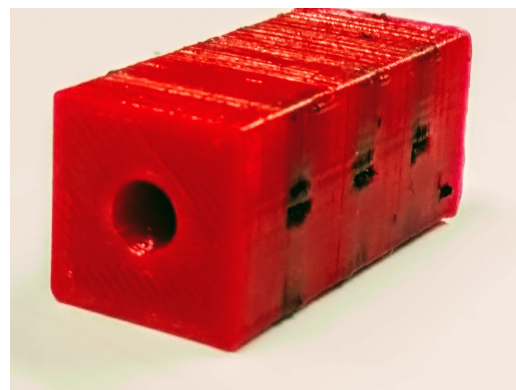


**Figure 4.1:** Proposed design of the sensors



**(a)** Version 1 sensor



**(b)** Version 2 sensor

**Figure 4.2:** Fabricated sensors with conductive part PI-eTPU 85 (black) and non conductive semiflex (red)

### 4.2 Fabrication of Sensor

For fabrication of the sensors a Flashforge Creator Pro FDM printer with Flexion extruder is used. FDM facilitates layer by layer printing of the components and hence the name additive manufacturing. CAD designs are made using Autodesk Fusion 360 and the slicer software Simplify3D to convert the CAD drawing into a printing pattern. The slicer program is used to calibrate the printing settings as the 3D printing conditions affect the print quality as well as electrical properties. First a layer of semi-flex was printed followed by eTPU-85 on top and so on as indicated in the Fig 4.3.

While printing the sensor it was observed that if the printing direction was horizontal the parts did not bond well to each other, whereas in the vertical direction the parts had good layer adhesion, moreover it was much easier to printed the sensor in the vertical direction, taking into consideration the circular cross section of the channel. Figure 4.3 shows the layered printing process of the sensor. Highlighted in green colour is semi-flex and in blue colour is PI-eTPU 85. The following Table 4.1 summarises the printer settings.

	PI-eTPU 85 700+	Semiflex
Printing Temperature(°C)	210	210
Heat Bed Temperature (°C)	50	50
Infill Percentage	100	95
Extrusion Multiplier	1.25	1.38
Retraction distance(mm)	10	8
Coasting (mm)	0.4	0.2
Printing speed(mm min <sup>-1</sup> )	2000	2000
Infill Pattern	Rectilinear	Rectilinear
Nozzle diameter(mm)	0.6	0.4

**Table 4.1:** Printing parameters

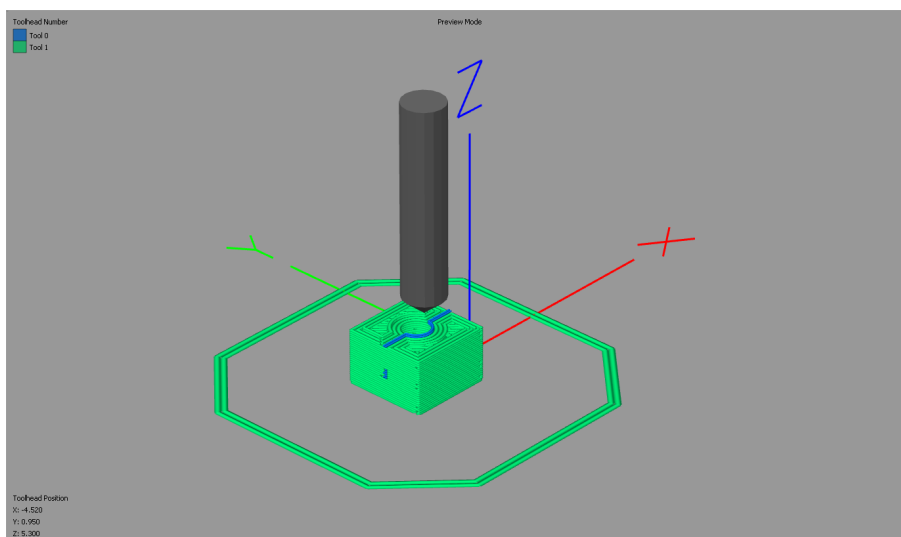


**Figure 4.3:** Direction of printing

## 5 Experimental Methods

In this Chapter the experimental setup to measure the response from the sensor will be discussed. Along with the setup, the protocols used to perform the experiment, flow profiles and the readout technique are also discussed.

### 5.1 Pressure driven flow

#### Experimental setup

The connections to the sensor are as shown in Figure 5.1. 3 mm diameter tubing was connected at the inlet and outlet of the sensor. A flow control valve (D) was used to regulate the pressure inside the channel and hence the flow. (A) and (E) are the inlet and discharge respectively. Power was supplied to the heater using a programmable DC power supply (F). Fig 5.1 represents Picoscope used for signal acquisition from the sensor using the voltage divider circuit as mentioned in Chapter 4. A silver conductive ink was applied at the contact pads for better connectivity. The ends of the tubing were sealed completely by using a hot glue to prevent leakage from the ends, and also to fix the sensor on the board.

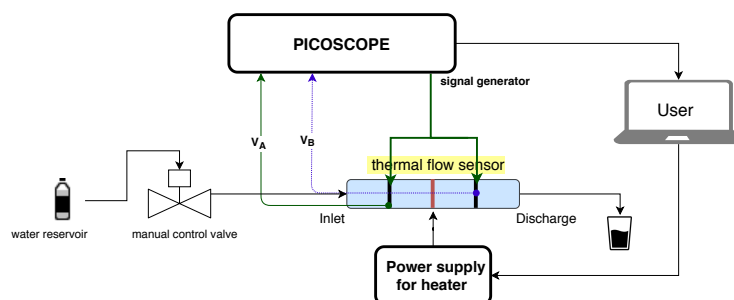


**Figure 5.1:** Pressure driven flow setup

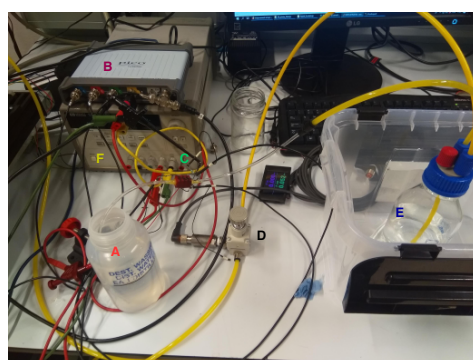


**Figure 5.2:** Pressure driven flow setup

#### Methods

The flow is actuated using a pressure driven pump as shown in the Figure 5.2. Outlet of the pump is connected to the inlet of the sensor and the outlet of the sensor channel is collected as discharge. The Picoscope 5000 series is used both as a signal generator and to measure the output of the bridge connection. The signal generator actuates the sensing resistors at an amplitude of 2V peak and a frequency of 2 kHz. Heat is generated by supplying power to the heater by means of a programmable DC power source unit (Agilent E3631A). The amount of

power delivered to the load (in this case the heater) is controlled by modulating the voltage ( $P_{\text{load}} = V^2/R_{\text{load}}$ ).

### Protocol

To characterise the sensor, the output voltage of the sensor is measured against the fluid flow. The volumetric fluid flow is translated from volume flow ( $\text{ml min}^{-1}$ ) to linear velocity<sup>1</sup> ( $\text{mm s}^{-1}$ ). The flow rates used in the experiment are indicated in Table 5.1.

Q ( $\text{ml min}^{-1}$ )	v ( $\text{mm s}^{-1}$ )
2	4.714
2.6	6.128
3.3	7.778

**Table 5.1:** Flow rates used in the Experiment

First, a test experiment was conducted using air as the medium. The same experiment was later repeated using deionised water water as the fluid medium. The heater power used in the experiment was varied between 40 mW to 170 mW. To observe the variation in the response two types of tests were conducted.

- Steady increase in heater power keeping the fluid velocity constant
- Switching the flow on-off at constant intervals keeping the flow rate steady.

## 5.2 Syringe pump setup

### Experimental setup

The experimental arrangement is as shown in Fig 5.4. 15 ml (D) BD syringe containing deionised water water was used as liquid medium loaded in the syringe pump apparatus (C). deionised water water was infused in the sensor (B) through the inlet and collected in a glass jar (A)

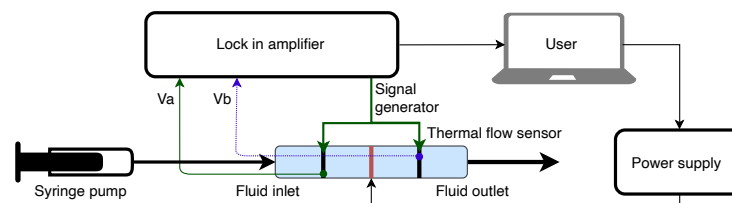


**Figure 5.3:** Syringe pump setup

### Methods

Figure 5.3 shows the actuation system using a syringe pump system (make Harvard Apparatus PHD Ultra). Syringes of 15 volume were loaded in the syringe pump, which acts as a liquid reservoir. Predetermined flows were set in the machine using the standard flow control GUI available. Parameters such as rate of flow, volume, time, direction were set. For the sensor measurement, the Picoscope was replaced by a Lock In Amplifier (SR830 Stanford systems). Sensing resistors were actuated using an in built signal generator at an amplitude of 1.5V peak and at a frequency of 1.5 kHz. The output of the voltage divider bridge was measured differentially with the help of a lock in amplifier. Output of the sensor was demodulated by adjusting the amplifier time constant to 10 ms and the roll off to 12dB.

<sup>1</sup> $Q = Av$



**Figure 5.4:** Syringe pump setup

### Protocol

Only the second version of the sensor was tested using the syringe pump setup using deionised water as the fluid medium. The initial resistances of the heater and sensor were measured before beginning the experiment. A flow control program was fed to the programmable syringe pump, such that the fluid would be injected in the channel at a specific flow rate. The flow rates used in the experiment were  $0 \text{ ml min}^{-1}$  to  $10 \text{ ml min}^{-1}$ .

Q ( $\text{ml min}^{-1}$ )	v ( $\text{mm s}^{-1}$ )
1	2.357
2	4.714
3	7.071
4	9.428
5	11.785
6	14.14
7	17
8	18.85
9	21.213
10	23.57

**Table 5.2:** Flow rates used in the Experiment

### 5.3 Readout Design

The sensing resistors are arranged in a voltage divider circuit as shown in Figure 5.5. A set of two fixed resistors  $R_{\text{fixed}}$  is used as voltage divider resistances. The value of the  $R_{\text{fixed}}$  is chosen such that the value is close to  $R_0$ . The output of the bridge  $V_{\text{ab}}$  is sensed by the same device used for signal generation, and is given as below.

$$\frac{\Delta R}{R_0} = \frac{V_{\text{ab}}}{V_{\text{in}}} \quad \text{where} \quad V_{\text{ab}} = (V_{\text{b}} - V_{\text{a}}) \quad \Delta R = R_{\text{down}} - R_{\text{up}} \quad (5.1)$$

$$V_{\text{a}} = V_{\text{in}} \left[ \frac{R_{\text{up}}}{R_{\text{up}} + R_{\text{fixed}}} \right] \quad (5.2)$$

$$\text{where } R_{\text{up}} = R_0 + \Delta T_{\text{up}} \alpha R_0 \quad (5.3)$$

$$V_b = V_{in} \left[ \frac{R_{down}}{R_{down} + R_{fixed}} \right] \tag{5.4}$$

where  $R_{down} = R_0 + \Delta T_{down} \alpha R_0$  (5.5)

$$V_{out} = V_b - V_a = V_{in} \left[ \frac{R_{down}}{R_{down} + R_{fixed}} - \frac{R_{up}}{R_{up} + R_{fixed}} \right] \tag{5.6}$$

Substituting the values of  $R_{down}$  and  $R_{up}$  from equation (5.3) and (5.5) in Equation (5.6)

$$V_{out} = V_b - V_a = V_{in} \left[ \frac{(\Delta T_d - \Delta T_u) \alpha}{2R_{fixed} + (\Delta T_d + \Delta T_u) \alpha} \right] \tag{5.7}$$

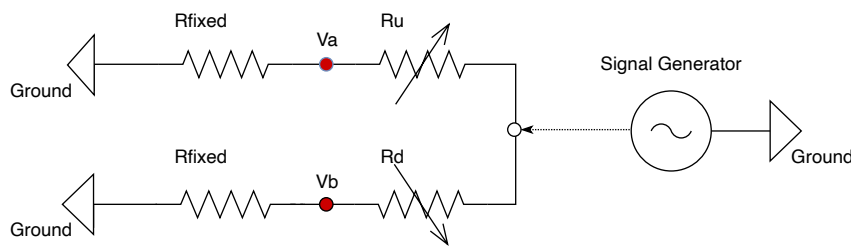


Figure 5.5: Readout Design

### 5.4 Signal Analysis

#### Lock in Measurement

Due to noise in the measurement data it is necessary to distinguish the signal of interest. Therefore, a lock in measurement technique is used to identify the signal of interest [44]. The lock in method was implemented by generating a reference signal (channel C of the Picoscope) from the signal generator and superimposing it on the channels A and B of the sensor as seen in Fig 5.6. Using this technique, the noisy signal from the sensor output was filtered using a low pass filter, and only the interested signal can be extracted as seen in Figure 5.7.

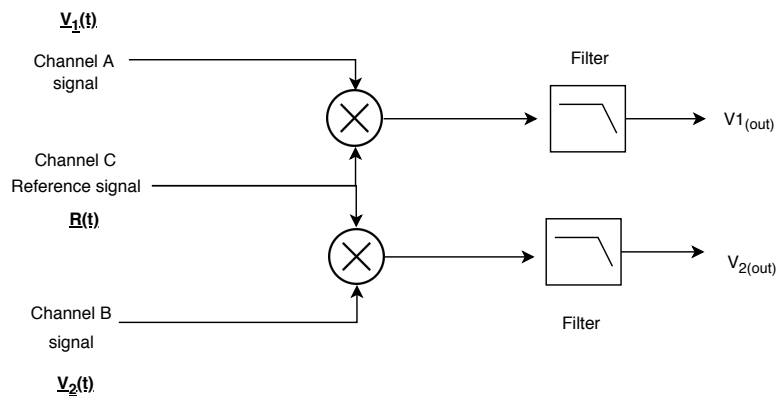
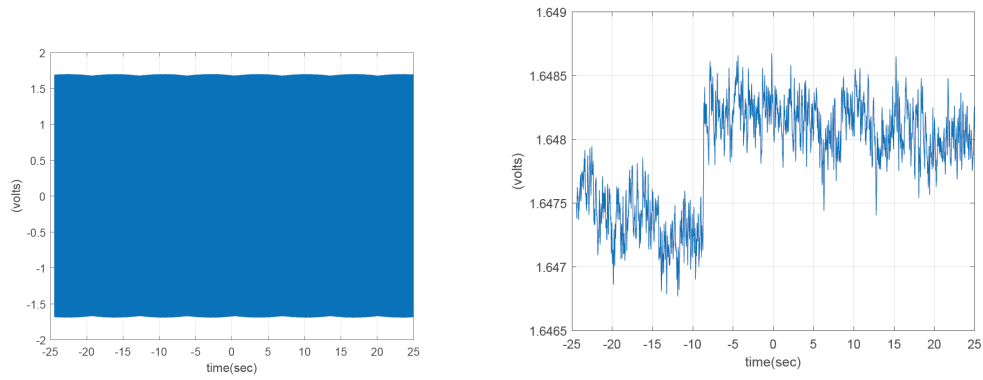


Figure 5.6: Lock in using Picoscope



**Figure 5.7:** Extraction of usable signal (*right*) from an extremely noisy signal(*left*) using lock in technique

## 5.5 Conclusion

The experimental methods have been discussed which consist of pressure driven and syringe pump setup along with a suitable voltage divider readout method. Signal analysis is performed using a lock in technique to determine the true signal of interest.

## 6 Results and Discussion

In this Chapter the results of the experiments performed on both the sensors are presented. Measurements using a pressure driven pump setup and a syringe pump setup will be discussed.

### 6.1 Pressure driven pump setup Measurements

The sensor Version 1 was tested for the flow measurements. Measurement setup used is discussed in the previous Chapter under Section 5.1. Series of tests were performed on the sensor with air and deionised water water as the fluid medium.

#### 6.1.1 Sensor with air as the medium

##### Methods

Before beginning with the flow experiments initial resistances of the sensors and heater were noted mentioned in Table 6.1.1. An external voltage divider resistor of value 3 k $\Omega$  was used as a fixed resistor. Recollecting the annealing experiments from Chapter 3, the sensor was annealed at a temperature of 140 °C for 6 hours in order to decrease its resistance. The heater power was regulated from 2 mW to 10 mW using a programmable DC power source by doing a voltage sweep from 5 V to 10 V. Here, the carrier(reference) signal of amplitude 2V and frequency 1 kHz was superimposed on each of the two channels A and B of the sensors. The outputs from the sensor are filtered using a low pass butter-worth filter to remove the noise from the measured signals.

##### Results

Location	After 3D printing k $\Omega$	After baking in Oven at 140 °C k $\Omega$
$R_{up}$	50.985	10.35
$R_{down}$	60.23	12.58
$R_{heater}$	50.269	10.34

Figure 6.1 shows the response of the sensor for the no flow condition using air as the medium. No significant changes were observed in the output measurements. A sudden spike was seen in the output response when the flow was switched on at ( $t = 10$  sec).

#### 6.1.2 Sensor with water as the medium

##### Methods

The empty channel was slowly filled with deionised water water without disturbing the previous setup. The sensor and heater resistances were measured again to ensure that the connections were tight. The power supplied to the heater was varied from 40 mW to 170 mW using a programmable DC power supply unit. A flow rate of 4 ml min<sup>-1</sup> was used in the experiment. Referring to Fig 6.1, at  $t = 0$  s the flow was induced in the channel with heater on, and at  $t = 130$  s the flow was turned off (each division on the time axis corresponds to 20 seconds).

##### Results

Figure 6.2 shows the response from the thermoresistive sensors. No change was noticed even if the flow was switched on at ( $t = 0$  sec) till ( $t = 120$  sec). However, when the flow was switched off, at ( $t = 125$  sec) a sharp declining trend is observed in the output response.

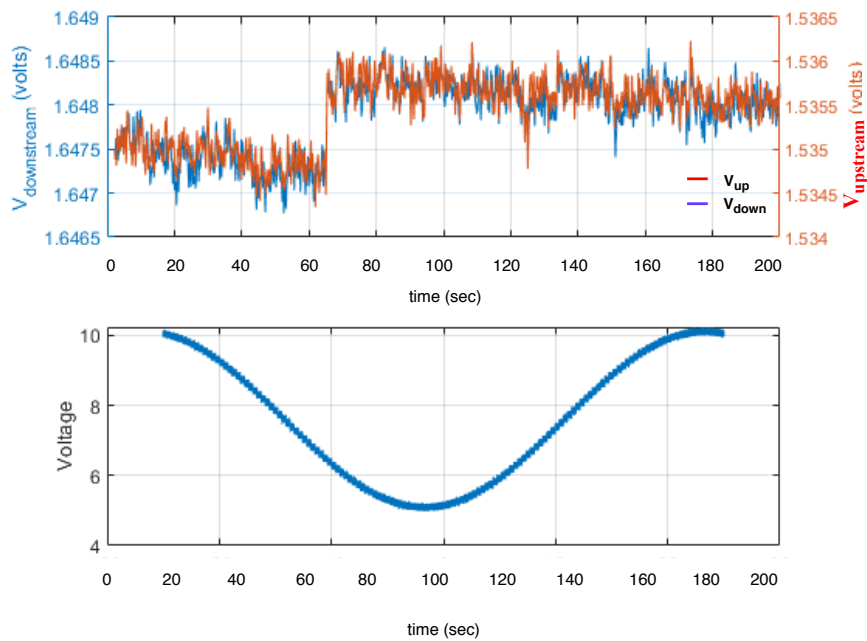


**Figure 6.1:** Sensor output with air in the channel (TOP) Output from the sensing resistors as a function of time, (DOWN) Modulated power in terms of change of voltage over time

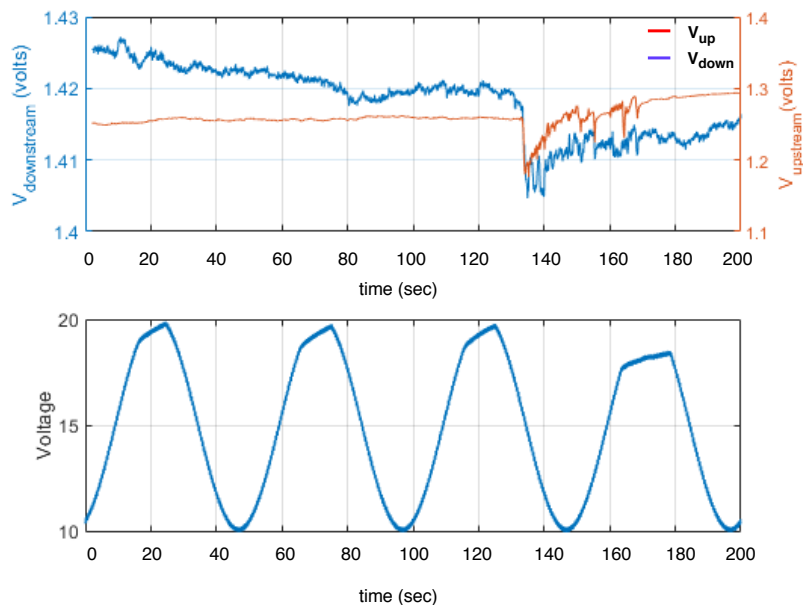


**Figure 6.2:** Sensor response with deionised water (TOP) Output from the sensing resistors as a function of time, (DOWN) Modulated power in terms of change of voltage over time

## Discussion

The power supplied to heater was not sufficient to heat the heater enough. When the heater temperature was measured using an RTD, the temperature rise achieved was only 5 °C degrees after supplying 500 mW of power. The reason for low power dissipation could be due to the high heater resistance. It was also noticed that, the channel was leaking at some points especially at the contact points of the tubing and sensor connections. Gluing the contacts using epoxy glue

did not help to solve the issue. The sensing leads were loosely attached to the sensor and hence improper connections lead to improper readings.

### 6.1.3 Steady Increase in Heater Power at constant velocity

#### Methods

Owing to the drawbacks of the sensor version 1 the new version of the sensor was tested in the following experiments. A similar lock in technique was used to detect usable signal, but now the difference between the downstream and upstream sensor output was plotted with respect to time to get a clear view of the experiment. The heater power was modulated in the range of 0 mW to 800 mW. The values of the new sensor and heater resistances are as mentioned below. The fluidic channel was filled with water, any visible air bubbles were completely removed by increasing the pressure inside the fluidic channel. The flow control valve was turned on to set the flow to a steady rate of  $10 \text{ mm s}^{-1}$ . The heater was turned on, gradually developing heat in the system. The heater power was varied from 0 mW to 500 mW.

Location	After 3D printing k $\Omega$	After baking in Oven at 140 °C k $\Omega$
$R_{\text{down}}$	8.68	0.72
$R_{\text{up}}$	7.25	0.73
$R_{\text{heater}}$	7.42	0.612

#### Results

The output response of the sensor is represented in the Figure 6.3 below

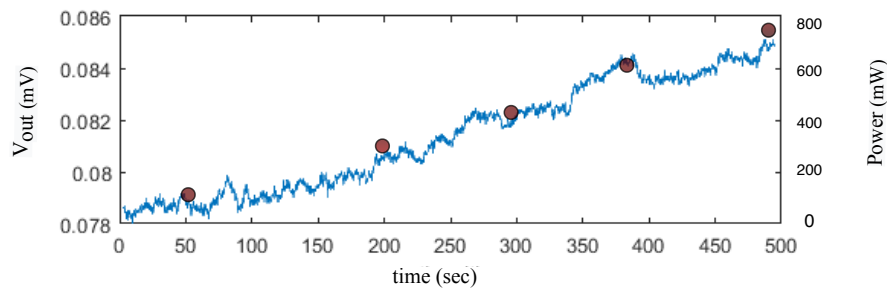


**Figure 6.3:** Sensor Response to increasing heater power

### 6.1.4 Alternate On-Off flow

#### Methods

Figure 6.4 describes the behaviour of the system when the flow is switched on and off alternately. The flow velocity was maintained at  $7 \text{ mm s}^{-1}$  when the flow was turned on.

#### Results

From Fig 6.4 at ( $t = 50 \text{ sec}$ ) it can be seen that the sensor begins to show an increasing trend in voltage output till about 175 sec at which the flow was turned off, leading to a declining trend in the graph. After ( $t = 175 \text{ sec}$ ) the sensor starts to cool. The most important observation is that the rise in temperature is proportional to both flow velocity and heater temperature.

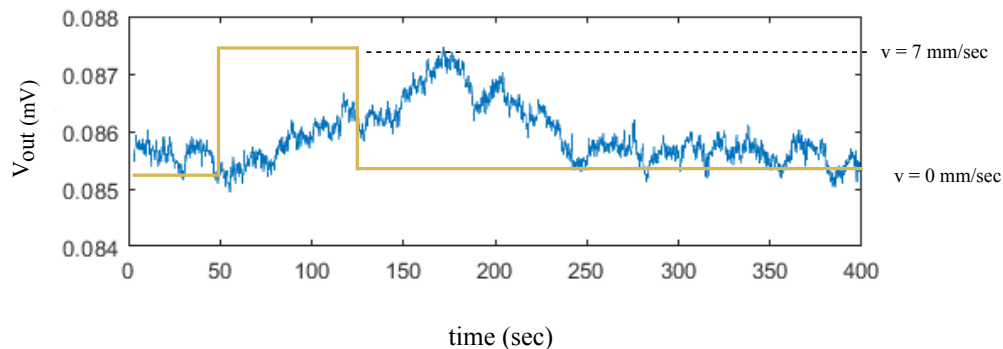


**Figure 6.4:** Sensor response to alternate on-off of flow

## 6.2 Syringe pump setup Measurements

### Methods

Sensor version 2 was used for the syringe pump measurements. The measured values of the upstream and downstream resistances were 1.224 k $\Omega$  and 1.220 k $\Omega$  respectively. The heater resistance was measured 1 k $\Omega$ . To see if the temperature rise in the heater was as per the modelled result the static characteristics of the heater element was first measured and compared Figure 6.5a shows the static characteristics of the heater element. A DC power supply was used to supply power to the heater ( $P = V^2/R_{\text{heater}}$ ). The rise in temperature of the heater was monitored using a thermocouple placed inside the channel. Power was increased gradually in steps of 2 V and the corresponding temperature rise was monitored.

Once the connections were made the heater was turned on monitoring the rise in temperature of the fluid (deionised water). A temperature rise was seen from 23  $^{\circ}\text{C}$  to 58  $^{\circ}\text{C}$ . Once the temperature was stabilised, the flow was turned on. Flow velocities of 0 ml min $^{-1}$  to 10 ml min $^{-1}$  were used in the flow control programme and the heater power was regulated at 1 W.

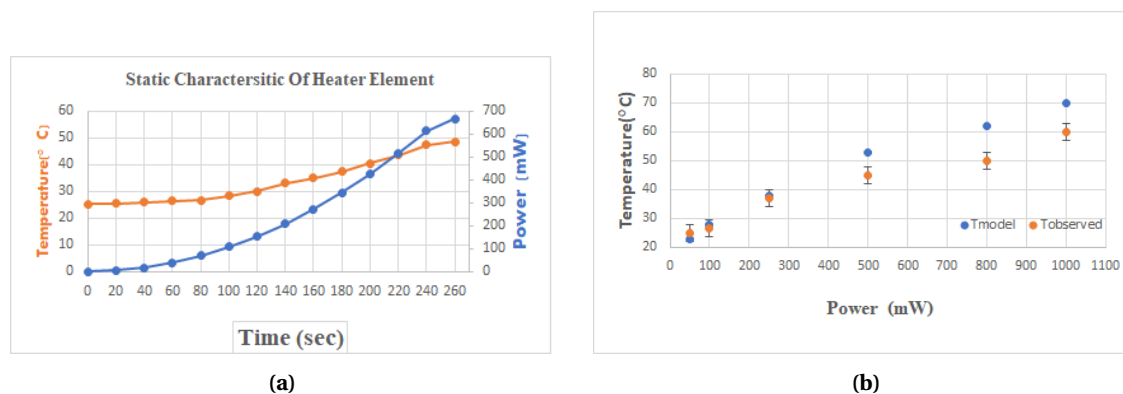


**Figure 6.5:** (left) static characteristic of heater element (right) model and observed results

### Results

Figure 6.5 shows the increase of temperature inside of the channel with increasing heater power. Before the start of the flow profile, the temperature increased from 23  $^{\circ}\text{C}$  to a stable 58  $^{\circ}\text{C}$  at a power of 1 W. The measured resistance of the upstream and downstream resistances were 1.224 k $\Omega$  and 1.220 k $\Omega$  respectively. The heater resistance was measured 1 k $\Omega$ .

Figure 6.6 shows the modelled and average output of the sensor with respect to the flow rate. For the model a TCR of  $\alpha = 0.024 \text{ }^{\circ}\text{C}^{-1}$  was taken. This figure shows a linear response of the

sensor to flow rates of about  $3 \text{ mLmin}^{-1}$  with a sensitivity of  $20 \text{ mV}/(\text{ml}/\text{min})$  with an  $1.5 \text{ V}$  input voltage.

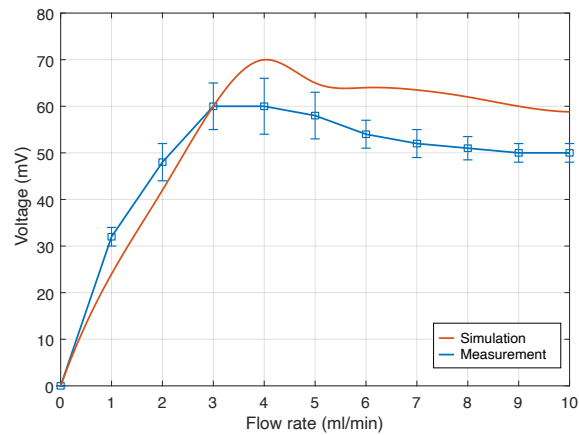


**Figure 6.6:** Sensor Response to increasing flow rate

### 6.2.1 Conclusion

The results from the syringe pump setup displayed better results than the pressure driven pump. At higher flow velocities the output voltage to flow rate relation flattens and subsequently reverses.

## 7 Conclusion

A 3D printed flow sensor concept has been modelled, characterised and fabricated successfully and the research questions discussed in Chapter 1 were addressed. The principle of thermal flow sensing in a 3D printed sensor was demonstrated.

Taking into account the previous work on modelling a calorimetric flow sensor, the analytical model described in the thesis has been successful in the current application for laminar flows. The model proved to be successful in estimating the optimal position of sensors. The current model also gives an estimation on sensor positioning to obtain maximum sensitivity which was incorporated while fabricating the sensor.

The resistance-temperature characteristics of the sensors were studied for thermo-resistive effects. The TCR of material was found to be high enough ( $0.024\text{ }^{\circ}\text{C}^{-1}$ ) to be used for (thermal) sensing applications. While characterising the sensor material, PI-eTPU 85 displayed both PTC as well as NTC effect at different temperature ranges. The origin of PTC and NTC effects in carbon doped conductive polymers is still a subject for further research and outside the scope of the current thesis. The annealing effect on the sensor material was studied and it was found that the resistance of the material decreased by a factor of 8 per heat cycle as seen in Chapter 3. The TCR of PI-eTPU displayed changes under the influence of temperature but found to be quite promising for thermal sensing applications.

The sensor was successfully 3D printed using an FDM printing process. The second prototype of the sensor with dimensions 15 mm x 12 mm x 12 mm showed promising results due to better design. The sensor displayed a sensitivity of  $24.84\text{ mV}/(\text{ml}/\text{min})$  over a flow ranging from  $0\text{ ml min}^{-1}$  to  $10\text{ ml min}^{-1}$ .

## 8 Future Work

In the future, the current analytical model could be extended for 3 dimensional geometry of the sensor to get a better picture on the thermal behaviour inside the sensor channel. The experimental and analytical results can be compared to numerical simulations to validate the models. An angular acceleration sensor can be characterised by rotating the sensor with varying frequency. A toroidal design of the channel can be chosen for 3D printing using current state of art 3D printed methods. More research can be perform on different conductive materials which can be used in sensing applications.

## A Appendix

### A.1 Constants derivation for time independent constant flow

Recollecting Equation 2.25 and 2.26 from Chapter 2

$$T(x) = \begin{cases} A_1 e^{\frac{\rho c_p v x}{k}} + B_1 & \text{for } -L \leq x \leq -x_h \\ C_1 e^{\frac{\rho c_p v x}{k}} & \text{for } |x| \leq -x_h \\ A_2 e^{\frac{\rho c_p v x}{k}} + B_2 & \text{for } x_h \leq x \leq L \end{cases} \quad (\text{A.1})$$

$$\begin{aligned} A_1 e^{-nL} + B_1 &= T_{\text{amb}} & x &= -L \\ A_1 e^{-nx_h} + B_1 &= C_1 e^{-nx_h} + C_2 - \frac{Qx_h}{nk} & x &= -x_h \\ A_1 n e^{-nx_h} &= C_1 n e^{-nx_h} + \frac{Qx_h}{nk} & x &= -x_h \\ A_2 e^{-nx_h} + B_2 &= C_1 e^{nx_h} + C_2 + \frac{Qx_h}{nk} & x &= x_h \\ A_2 n e^{nx_h} &= C_1 n e^{nx_h} + \frac{Qx_h}{nk} & x &= x_h \\ A_2 e^{nL} + B_2 &= T_{\text{amb}} & x &= L \end{aligned} \quad (\text{A.2})$$

From the above relation

$$A_2 e^{nx_h} - A_1 e^{-nx_h} + A_1 e^{-nL} - A_2 e^{nL} = C_1 e^{nx_h} + -C_1 e^{-nx_h} + 2 \frac{Qx_h}{nk} \quad (\text{A.3})$$

$$A_2 n e^{nx_h} - A_1 n e^{-nx_h} = C_1 e^{nx_h} - C_1 e^{-nx_h} \quad (\text{A.4})$$

$$A_1 = 2 \frac{Qx_h}{nke^{-nL}} + A_2 e^{2nL} \quad (\text{A.5})$$

$$A_1 - A_2 = \frac{Q}{n^2 k e^{-nx_h}} - \frac{Q}{n^2 k e^{nx_h}} \quad (\text{A.6})$$

$$A_2 = \frac{Q(e^{-n(L-x_h)} - e^{-n(L+x_h)} - 2x_h)}{n^2 k (e^{nL} - e^{-nL})} \quad (\text{A.7})$$

$$A_2 = \frac{Q(e^{n(L+x_h)} - e^{n(L-x_h)} - 2x_h)}{n^2 k (e^{nL} - e^{-nL})} \quad (\text{A.8})$$

$$C_1 = \frac{Q(e^{-n(L-x_h)} - e^{n(L-x_h)} - 2x_h)}{n^2 k (e^{nL} - e^{-nL})} \quad (\text{A.9})$$

$$B_1 = T_{\text{amb}} - A_1 e^{-nL} \quad B_2 = T_{\text{amb}} - A_2 e^{nL}$$

$$B_2 = T_{\text{amb}} - \frac{-Qe^{nL}(e^{-n(L-x_h)} - e^{-n(L+x_h)} - 2x_h)}{n^2 k (e^{nL} - e^{-nL})} \quad (\text{A.10})$$

$$B_1 = T_{\text{amb}} - \frac{-Qe^{nL}(e^{n(L+x_h)} - e^{-n(L-x_h)} - 2x_h)}{n^2 k (e^{nL} - e^{-nL})} \quad (\text{A.11})$$

## A.2 Effect Of Printing direction on the resistivity

Next, the effect of printing direction on the resistivity of 3D printed eTPU- 85 was studied by changing the length, width and height of samples respectively. Figure A.3 shows the effect of changing lengths on the resistance vs temperature curves of a 20 mm and 21mm printed filament. The resistance and hence resistivity increases with increase in length of the printed sample with an average resistance change by a factor of 2 when the length was increased by 1mm . Large hysteresis was observed in the larger sample. The rate of change of resistance was quite high in case of the larger sample with an average change in resistance of 10 k $\Omega$  per 10  $^{\circ}$ C rise in temperature.

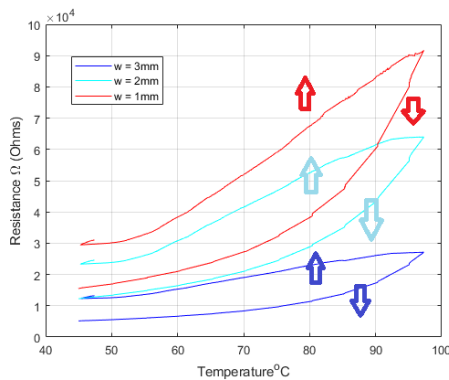


Figure A.1: Change in widths

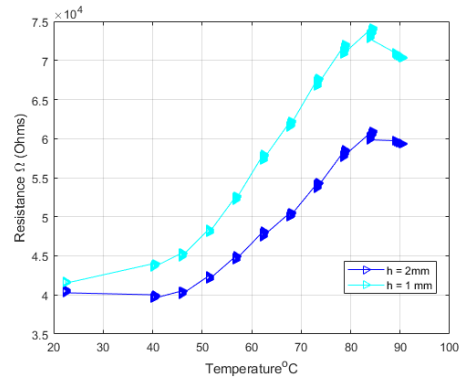


Figure A.2: Change in layer height 1 mm and 2 mm

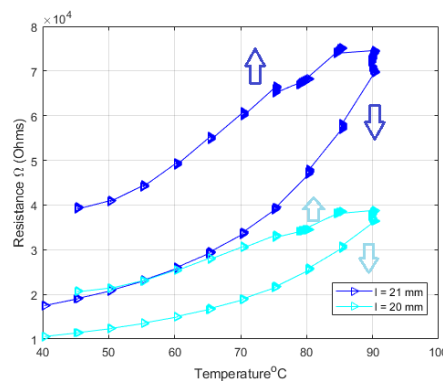


Figure A.3: Effect of length change

Figure A.1 shows the effect of changing widths. Resistivity was seen to decrease with increasing layer width with larger hysteresis observed in sample of least width. The length of the sample was kept constant at 20 cm. Results from variation of layer height show that as the layer height increases the resistivity decreases as seen in Figure A.2

## A.3 Abstract IEEE SENSORS

# 3D-Printed Calorimetric Flow Sensor

Gerjan Wolterink<sup>1,2</sup>, Ameya Umrani<sup>1</sup>, Martijn Schouten<sup>1</sup>, Remco Sanders<sup>1</sup>, Gijs Krijnen<sup>1</sup>

<sup>1</sup>Robotics And Mechatronics group, <sup>2</sup>Biomedical Signal and Systems

University of Twente, Enschede, The Netherlands, Email: gerjan.wolterink@utwente.nl

**Abstract** - This paper shows the development and characterization of a fully 3D-printed thermal mass flow sensor, based on regular and carbon-doped thermoplastic polyurethane (TPU). Using multi material fused deposition modelling (FDM) 3D-printing, the sensor is based on one heater element and two resistive thermal sensors (sensor - heater - sensor configuration). The transduction is based on the well-known temperature dependent resistance of carbon doped polymers. Characterisation of the conductive TPU shows a positive thermal coefficient of resistance (TCR) ranging between  $0.002\text{ }^{\circ}\text{C}^{-1}$  to  $0.024\text{ }^{\circ}\text{C}^{-1}$ , whereas the sensor shows a responsivity of  $20\text{ mV ml}^{-1}\text{ min}^{-1}$  in the pseudo linear range for flows below  $3\text{ mL min}^{-1}$  while using a power of  $1\text{ W}$  and heating up  $58\text{ }^{\circ}\text{C}$ .

*Keywords* - 3D-Printing, Calorimetric, Flow Sensing, FDM, Conductive TPU

## I. INTRODUCTION

3D-printed sensors are of interest for small volume, distributed fabrication, customisation and integration in 3D-printed structures. These advantages also count for microfluidic structures due to a small number of required fabrication steps to create 3D geometries and customisation at low cost. 3D-printing also allows for the creation of functional sensing structures that can be embedded in microfluidic structures [1], [2]. A 3D-printed Venturi tube for flow sensing has been demonstrated by Ademski et al. [1], Leigh et al. [3] have demonstrated an impeller flow sensor made using fused deposition modeling (FDM) technology. However both methods are hybrid approaches and additional commercial sensors needed to be placed inside the structure. Recently a 3D printed flow sensor, with additional metallization, based on the Coriolis effect was presented [4].

In this work we show a proof of concept calorimetric flow sensor, completely fabricated using a consumer grade multi-material FDM 3D-printer. It does not need additional sensors since the conductive material functions as heater and sensor. Previously reported 3D printed sensors printed in one go using FDM technology are mainly resistive and capacitive force sensors and do not use the thermal properties of the conductive material [5]–[10].

## II. SENSOR PRINCIPLE

### A. Calorimetric Flow Sensing

In calorimetric flow sensing, heat is injected in a flow and the corresponding temperature change due to convection is measured at a certain distance. One implementation uses two

thermal sensors and a heater. Relative to the flow-direction, one sensor is placed upstream, whereas the second one is located downstream [11], [12]. The heat is carried away from the heater by the flow in the direction of the flow. The thermal gradient causes the upstream temperature to fall and the downstream temperature to rise.

The heating is simply by joule heating, resulting in a temperature increase in the fluid, the heat of which subsequently is carried away by the flow. The resistance of the sensors are sensitive to temperature and in a certain flow range the difference in temperature is resolved as a resistance difference proportional to the heat transported by the flow. As such it is a direct measurement of the heat flow, and an indirect measurement of fluid velocity [11]. The working of the calorimetric flow sensing is illustrated in Figure 1.

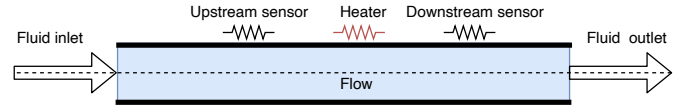


Fig. 1. Schematic representation of a calorimetric flow sensor.

### B. Model

In our sensor geometry the flow is unidirectional through a circular duct formed in a 3D printed structure which consists of two concentric sensors and one concentric heater, see Figure 2 left. We consider a one-dimensional heat transfer model with flow velocity and temperature averaged over the cross-section.

$$\rho c_p \left[ \frac{\partial T}{\partial t} + v \frac{\partial T}{\partial x} \right] - k \frac{\partial^2 T}{\partial x^2} = \frac{Q(x)}{A} \quad (1)$$

Where  $c_p$  is the specific heat,  $\rho$  the fluid density,  $k$  the thermal conductivity of the fluid,  $v$  the average velocity of the flow in  $x$ -direction,  $A$  the cross-section of the tube and  $Q$  the heat density, which is only non-zero at the position of the heater. Introducing boundary conditions at the edges of the heater and assuming the temperature at the ends of the sensor structure to be at ambient temperature, for time independent flow the solution to the simplified system reads:

$$T(x, v) = \begin{cases} A_1 e^{\rho c_p x/k} + B_1, & -L \leq x \leq -x_h \\ \frac{1}{\rho c_p v} [A_c k e^{\rho c_p x/k} + Qx] + B_c, & |x| \leq x_h \\ A_2 e^{\rho c_p x/k} + B_2, & x_h \leq x \leq L \end{cases} \quad (2)$$

where  $2L$  is the length of the sensor,  $x_h$  is half the heater length and  $A_i$  and  $B_i$ ,  $i = 1, 2, c$  implicitly depend on  $v$ .

Figure 2 shows the effect of the  $v$  on the temperature inside the tube for deionized water.  $v$  ranges from  $0\text{ mm s}^{-1}$  to

$100 \text{ mm s}^{-1}$  assuming a constant power of 300 mW supplied to the heater.

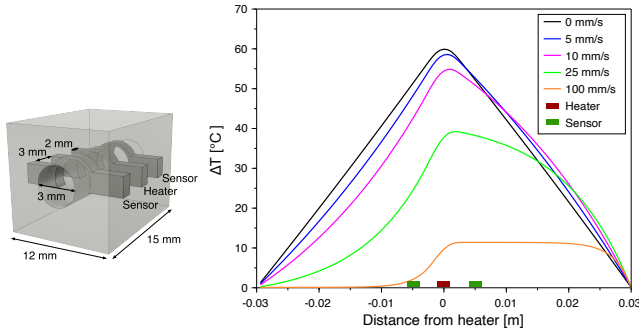


Fig. 2. Left: CAD file of the sensor. Right: temperature profile for various flow velocities.

### III. METHODOLOGY

#### A. Sensor design and Fabrication

Figure 2 left shows the CAD file of the flow sensor with a total length of 20 mm, the diameter of the circular channel is 3 mm. The heater is located at the centre of the channel and has a width of 2 mm the two sensors also have a width of 2 mm and are placed symmetrically at a 3 mm distance from the heater. The location of the sensing resistors is chosen based on the analytical expression eq. 2. The rectangular outside allowed for easy printing without the need for support material. The flow sensor is printed using a dual nozzle FDM 3D-printer (Creator Pro, FlashForge Corporation, China) fitted with a dedicated extrusion system for flexible materials (Flexion Extruder, Diabase Engineering, USA). The sensors and heaters are made of conductive TPU (PI-ETPU 85-700+, Palmiga Innovation, Sweden), the rest of the flow sensor structure is printed from non-conductive TPU (NinjaFlex SemiFlex, Fenner Drives, USA).

#### B. Thermal characterisation of conductive TPU

To determine the thermal properties of the conductive TPU material a 10 cm sample with a diameter 1.75 mm was placed in a computer controlled oven. The temperature was increased from  $40^\circ\text{C}$  to  $120^\circ\text{C}$  and back to  $50^\circ\text{C}$  over the course of 3 h. The sample was connected in a 4-wire configuration to a data acquisition unit (34970A, Keysight, USA). Conductive silver glue (SCP, Electrolube, UK) was used to make a connection between the sample and the copper tape traces that are connected to the data acquisition unit. To get insight in the repeatability of this measurement a heating cycle from  $30^\circ\text{C}$  to  $70^\circ\text{C}$  and back over the course of 3 hours was repeated for 4 cycles.

#### C. Flow sensor characterisation

Figure 3 shows a schematic representation of the measurement setup. The flow was provided by a programmable syringe pump (PHD Ultra, Harvard Apparatus, USA) using syringes with a volume of 15 mL. The flow sensor setup was filled with

deionized water, excess of water was collected by a container at the end of the flow sensor.

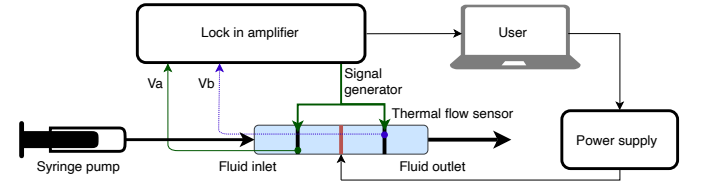


Fig. 3. Measurement setup,  $V_a$  and  $V_b$  represent the output of upstream and downstream thermal sensors.

The thermal sensors were connected in a voltage divider setup (Figure 4) and read out using a Lock-In Amplifier (SR830 Stanford systems), utilising its signal generator at an amplitude of 1.5 V and at a frequency of 1.5 kHz. The lock in time constant was set to 10 ms and the roll off to 12 dB. The output voltage is given by eq. 4 with  $R_u$  and  $R_d$  being the up- and downstream sensors and  $R_{\text{fixed}}$  fixed resistors of the voltage divider.

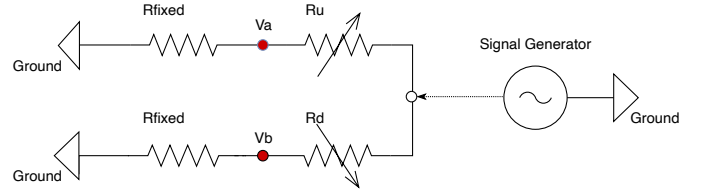


Fig. 4. Voltage divider readout circuit design,  $R_u$  and  $R_d$  are representing the upstream and downstream thermal sensors.

The output of the sensor can be simulated by modelling the resistance change of the upstream and downstream sensors:

$$R_u = R_0 + \Delta T_u \alpha R_0 \quad R_d = R_0 + \Delta T_d \alpha R_0 \quad (3)$$

With  $\Delta T$  the change in resistance and  $\alpha$  the temperature coefficient of resistance (TCR). The resulting expression for  $V_{\text{out}}$  is:

$$V_{\text{out}} = V_b - V_a = V_{\text{in}} \left[ \frac{(\Delta T_d - \Delta T_u) \alpha}{2R_{\text{fixed}} + (\Delta T_d + \Delta T_u) \alpha} \right] \quad (4)$$

For the the static characteristics of the heater element, the power was increased gradually in steps of 2 V ( $P = V^2/R_{\text{heater}}$ ). The corresponding temperature rise was monitored using a thermocouple placed inside of the channel.

To characterise the output of the sensor with respect to the flow rate, the power of the heater was regulated at 1 W, once the temperature was stabilised, the flow was turned on. The flow was increased in steps of  $1 \text{ ml min}^{-1}$  to a maximum of  $10 \text{ ml min}^{-1}$ , due to the limited volume of the syringe each flow velocity was measured separately. This measurement is repeated 5 times.

## IV. RESULTS

#### A. Thermal characterisation

Figure 5 shows the change in resistance with respect to temperature. A positive temperature coefficient (PTC) effect

was observed till  $110^{\circ}\text{C}$  after which the negative temperature coefficient (NTC) effect was seen up till the measurement limit of  $120^{\circ}\text{C}$ . From Figure 5 (big figure) the non-linear relation of the TCR with respect to temperature can be derived. It displays a superlinear rise from  $0.002^{\circ}\text{C}^{-1}$  till a maximum of  $0.024^{\circ}\text{C}^{-1}$  at  $110^{\circ}\text{C}$ .

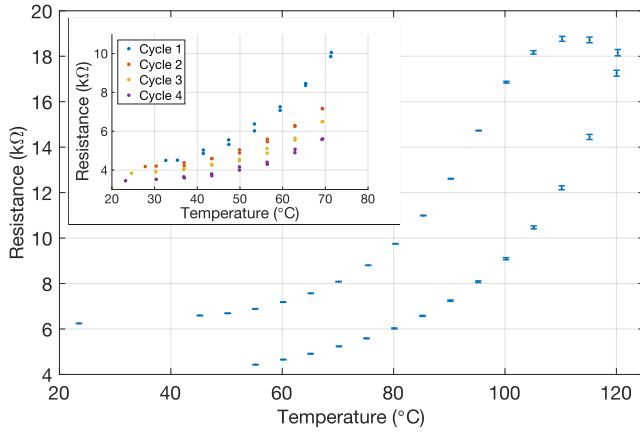


Fig. 5. Resistance over to a 3 hour heating cycle. Insert: Resistance change of four successive heating cycles over 3 hours.

The inset of Figure 5 shows that the resistance dropped after each cycle. However, the influence of temperature on the material is retained and hence can be used for temperature sensitive applications.

### B. Flow sensor characterisation

Figure 6 shows the increase of temperature inside of the channel with increasing heater power. Before the start of the flow profile, the temperature increased from  $23^{\circ}\text{C}$  to a stable  $58^{\circ}\text{C}$  at a power of 1 W. The measured resistance of the upstream and downstream resistances were  $1.224\text{ k}\Omega$  and  $1.220\text{ k}\Omega$  respectively. The heater resistance was measured  $1\text{ k}\Omega$ .

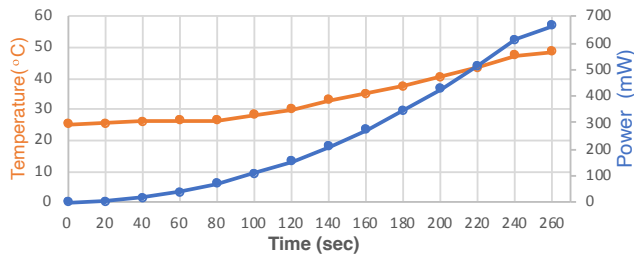


Fig. 6. Temperature in the channel at zero flow with increasing heater power.

Figure 7 shows the modelled and average output of the sensor with respect to the flow rate. For the model a TCR of  $\alpha = 0.024^{\circ}\text{C}^{-1}$  was taken. This figure shows a linear response of the sensor to flow rates of about  $3\text{ mL min}^{-1}$  with a sensitivity of  $20\text{ mV}/(\text{ml}/\text{min})$  with an  $1.5\text{ V}$  input voltage. At higher flow velocities the output voltage to flow rate relation flattens and subsequently reverses.

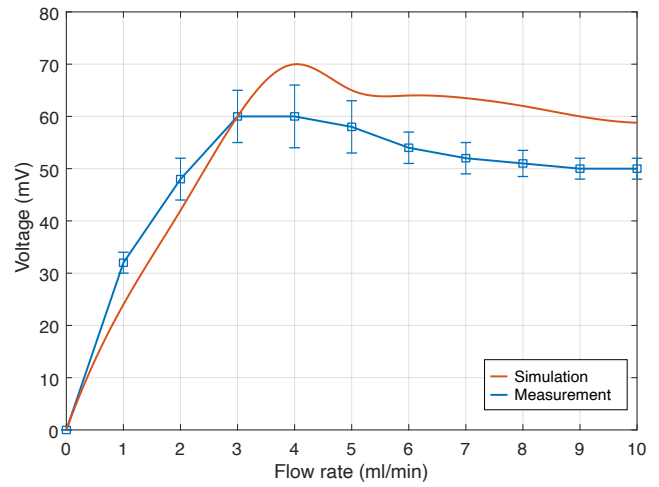


Fig. 7. Model and sensor response to increasing flow rate, measurements are an average over 5 recording, error bars indicate the lowest and highest value.

## V. DISCUSSION

Figure 5 shows a positive temperature coefficient (PTC) till  $110^{\circ}\text{C}$  after which the temperature coefficient becomes negative (NTC). This effect has been reported typically for polymer carbon composites. The PTC effect is thought to be caused by the difference in expansion coefficient between matrix and carbon black filler. Whereas the NTC is assumed to be the result of the formation of conducting networks at higher temperatures, the elastic modulus of the polymer matrix decreases leading to re-connection of the conductive pathways of the filler matrix [13], [14]

The hysteresis shown in Figure 5 might be caused by the thermal capacity of the material causing the cooling of the material to be slower than the environment temperature of the oven. Another explanation could be the annealing effect as show in Figure 5, resulting in a lower resistivity after multiple cycles. A high TCR is desired for sensitive temperature sensing, in comparison the TCR of platinum is  $0.0039^{\circ}\text{C}^{-1}$  [15], whereas the TCR of PI-eTPU could be as high as  $0.024^{\circ}\text{C}^{-1}$ . In the current design the usable range of the sensor is limited to a flow of  $3\text{ mL min}^{-1}$ . However, by changing the design the sensor can be tuned to a desired range. An application of these flow sensors could be in a 3D-Printed angular acceleration sensor based on the human vestibular system such as demonstrated by van Tiem et. al. [16].

## VI. CONCLUSIONS

To our knowledge, we have fabricated the first fully 3D-Printed calorimetric flow sensor using FDM technology that uses a conductive filament (PI-eTPU) as both sensing and heater material. The sensor has a close to linear output for flows below  $3\text{ mL min}^{-1}$  and has a sensitivity of  $20\text{ mV}/(\text{ml}/\text{min})$ . The TCR of PI-eTPU does vary under the influence of temperature but was found to be sufficient to be used for thermal sensing applications.

## REFERENCES

- [1] K. Adamski, B. Kawa, and R. Walczak, "Inkjet 3d printed venturi microflowmeter," in *2018 XV International Scientific Conference on Optoelectronic and Electronic Sensors (COE)*. IEEE, 2018, pp. 1–3.
- [2] L. G. Pagani, P. Carulli, V. Zega, R. Suriano, R. Bernasconi, A. Frangi, M. Levi, L. Magagnin, and G. Langfelder, "The first three-dimensional printed and wet-metallized coriolis mass flowmeter," *IEEE Sensors Letters*, vol. 4, no. 6, pp. 1–4, 2020.
- [3] S. Leigh, C. Purssell, D. Billson, and D. Hutchins, "Using a magnetite/thermoplastic composite in 3d printing of direct replacements for commercially available flow sensors," *Smart materials and structures*, vol. 23, no. 9, p. 095039, 2014.
- [4] L. Gaffuri Pagani, P. Carulli, V. Zega, R. Suriano, R. Bernasconi, A. Frangi, M. Levi, L. Magagnin, and G. Langfelder, "The first three-dimensional printed and wet-metallized coriolis mass flowmeter," *IEEE Sensors Letters*, vol. 4, no. 6, pp. 6–9, 2020.
- [5] M. Schouten, R. Sanders, and G. Krijnen, "3D printed flexible capacitive force sensor with a simple micro-controller based readout," in *2017 IEEE SENSORS*, Oct 2017, pp. 1–3.
- [6] S. J. Leigh, R. J. Bradley, C. P. Purssell, D. R. Billson, and D. A. Hutchins, "A simple, low-cost conductive composite material for 3d printing of electronic sensors," *PloS one*, vol. 7, no. 11, p. e49365, 2012.
- [7] M. B. Kirkpatrick, J. A. Tarbuton, T. Le, and C. Lee, "Characterization of 3d printed piezoelectric sensors: Determination of d 33 piezoelectric coefficient for 3d printed polyvinylidene fluoride sensors," in *SENSORS, 2016 IEEE*. IEEE, 2016, pp. 1–3.
- [8] A. Dijkshoorn, P. Werkman, M. Welleweerd, G. Wolterink, B. Eijking, J. Delamare, R. Sanders, and G. J. Krijnen, "Embedded sensing: integrating sensors in 3-d printed structures," *Journal of Sensors and Sensor Systems*, vol. 7, no. 1, p. 169, 2018.
- [9] G. Wolterink, R. Sanders, and G. Krijnen, "Thin, flexible, capacitive force sensors based on anisotropy in 3d-printed structures," in *2018 IEEE SENSORS*. IEEE, 2018, pp. 1–4.
- [10] —, "A flexible, three material, 3d-printed, shear force sensor for use on finger tips," in *2019 IEEE SENSORS*. IEEE, 2019, pp. 1–4.
- [11] Y.-H. Wang, C.-P. Chen, C.-M. Chang, C.-P. Lin, C.-H. Lin, L.-M. Fu, and C.-Y. Lee, "Mems-based gas flow sensors," *Microfluidics and nanofluidics*, vol. 6, no. 3, p. 333, 2009.
- [12] W. Xu, B. Gao, Y.-K. Lee, and Y. Chiu, "Packaging effect on the flow separation of cmos thermoresistive micro calorimetric flow sensors," in *2016 IEEE 11th Annual International Conference on Nano/Micro Engineered and Molecular Systems (NEMS)*. IEEE, 2016, pp. 62–65.
- [13] H. Tang, X. Chen, and Y. Luo, "Studies on the ptc/ntc effect of carbon black filled low density polyethylene composites," *European polymer journal*, vol. 33, no. 8, pp. 1383–1386, 1997.
- [14] C. Klason and J. Kubat, "Anomalous behavior of electrical conductivity and thermal noise in carbon black-containing polymers at tg and tm," *Journal of Applied Polymer Science*, vol. 19, no. 3, pp. 831–845, 1975.
- [15] K. Tsutsumi, A. Yamashita, and H. Ohji, "The experimental study of high tcr pt thin films for thermal sensors," in *SENSORS, 2002 IEEE*, vol. 2. IEEE, 2002, pp. 1002–1005.
- [16] J. van Tiem, J. Groenesteijn, R. Sanders, and G. Krijnen, "3d printed bio-inspired angular acceleration sensor," in *2015 IEEE SENSORS*. IEEE, 2015, pp. 1–4.

## Bibliography

- [1] J. K. Stroble, R. B. Stone, and S. E. Watkins, "An overview of biomimetic sensor technology," *Sensor Review*, vol. 29, no. 2, pp. 112–119, 2009.
- [2] G. J. Krijnen and R. G. Sanders, "Recent developments in bio-inspired sensors fabricated by additive manufacturing technologies," in *Advances in science and technology*, vol. 100, pp. 197–206, Trans Tech Publ, 2017.
- [3] P. Westerik, E. Berenschot, and G. Krijnen, "Development of a biomimetic eardrum for acoustic sensing," in *2015 IEEE SENSORS*, pp. 1–4, IEEE, 2015.
- [4] B. Eijking, R. Sanders, and G. Krijnen, "Development of whisker inspired 3d multi-material printed flexible tactile sensors," in *2017 IEEE SENSORS*, pp. 1–3, IEEE, 2017.
- [5] J. M. Goldberg, V. J. Wilson, D. E. Angelaki, K. E. Cullen, J. Buttner-Ennever, and K. Fukushima, *The vestibular system: a sixth sense*. Oxford University Press, 2012.
- [6] P. R. Adina T. Micheal Titus, *The Nervous System*. Systems Of the body Series, Elsevier Health Sciences, 2010.
- [7] L. S. Parnes, S. K. Agrawal, and J. Theriault, *Benign Paroxysmal Positional Vertigo*, pp. 290–303. Berlin, Heidelberg: Springer Berlin Heidelberg, 2013.
- [8] P. Selva, Y. Gourinat, and J. Morlier, "A matlab/simulink model of the inner ear angular accelerometers sensors," in *ASME 2009 International Design Engineering Technical Conferences and Computers and Information in Engineering Conference*, pp. 241–246, American Society of Mechanical Engineers Digital Collection, 2009.
- [9] R. D. Rabbitt, E. R. Damiano, and J. W. Grant, "Biomechanics of the semicircular canals and otolith organs," in *The vestibular system*, pp. 153–201, Springer, 2004.
- [10] H. Alrowais, P. Getz, M.-g. Kim, J.-J. Su, R. Tran, W. A. Lam, and O. Brand, "Bio-inspired fluidic thermal angular accelerometer with inherent linear acceleration rejection," *Sensors and Actuators A: Physical*, vol. 279, pp. 566–576, 2018.
- [11] J. Groenesteijn, H. Droogendijk, M. J. de Boer, R. G. Sanders, R. J. Wiegerink, and G. J. Krijnen, "An angular acceleration sensor inspired by the vestibular system with a fully circular fluid-channel and thermal read-out," in *2014 IEEE 27th International Conference on Micro Electro Mechanical Systems (MEMS)*, pp. 696–699, IEEE, 2014.
- [12] J. van Tiem, J. Groenesteijn, R. Sanders, and G. Krijnen, "3d printed bio-inspired angular acceleration sensor," in *2015 IEEE SENSORS*, pp. 1–4, IEEE, 2015.
- [13] Y. Xu, X. Wu, X. Guo, B. Kong, M. Zhang, X. Qian, S. Mi, and W. Sun, "The boom in 3d-printed sensor technology," *Sensors*, vol. 17, no. 5, p. 1166, 2017.
- [14] M. Schouten, "Towards additively manufactured complex robotic systems," Master's thesis, University of Twente, 2017.
- [15] M. Schouten, R. Sanders, and G. Krijnen, "3d printed flexible capacitive force sensor with a simple micro-controller based readout," in *2017 IEEE SENSORS*, pp. 1–3, IEEE, 2017.
- [16] G. Wolterink, R. Sanders, and G. Krijnen, "Thin, flexible, capacitive force sensors based on anisotropy in 3d-printed structures," in *2018 IEEE SENSORS*, pp. 1–4, IEEE, 2018.

- [17] C. Manganiello, D. Naso, F. Cupertino, O. Fiume, and G. Percoco, "Investigating the potential of commercial-grade carbon black-filled tpu for the 3d printing of compressive sensors," *Micromachines*, vol. 10, no. 1, p. 46, 2019.
- [18] G. Wolterink, R. Sanders, F. Muijzer, B.-J. van Beijnum, and G. Krijnen, "3d-printing soft semg sensing structures," in *2017 IEEE SENSORS*, pp. 1–3, IEEE, 2017.
- [19] Wikipedia contributors, "Louis vessot king — Wikipedia, the free encyclopedia," 2018. [Online; accessed 14-August-2019].
- [20] Wikipedia contributors, "Thermal mass flow meter — Wikipedia, the free encyclopedia," 2019. [Online; accessed 14-August-2019].
- [21] B. Khan, S. Ahmed, and V. Kakkar, "A comparative analysis of thermal flow sensing in biomedical applications," *arXiv preprint arXiv:1608.03603*, 2016.
- [22] J. T. Kuo, L. Yu, and E. Meng, "Micromachined thermal flow sensors—a review," *Micromachines*, vol. 3, no. 3, pp. 550–573, 2012.
- [23] S. Beeby, G. Ensel, N. M. White, and M. Kraft, *MEMS mechanical sensors*. Artech House, 2004.
- [24] Y.-H. Wang, C.-P. Chen, C.-M. Chang, C.-P. Lin, C.-H. Lin, L.-M. Fu, and C.-Y. Lee, "Mems-based gas flow sensors," *Microfluidics and nanofluidics*, vol. 6, no. 3, p. 333, 2009.
- [25] W. Xu, B. Gao, Y.-K. Lee, and Y. Chiu, "Packaging effect on the flow separation of cmos thermoresistive micro calorimetric flow sensors," in *2016 IEEE 11th Annual International Conference on Nano/Micro Engineered and Molecular Systems (NEMS)*, pp. 62–65, IEEE, 2016.
- [26] A. Arevalo, E. Byas, and I. G. Foulds, "Simulation of thermal transport based flow meter for microfluidics applications," in *2013 COMSOL Conference, Rotterdam, Holland*, 2013.
- [27] J. G. Webster, *The Measurement Instrumentation And Sensors Handbook*. Electrical Engineering Handbook, CRC Press, 2014.
- [28] R. B. Bird, W. E. Stewart, and E. N. Lightfoot, "Transport phenomena john wiley sons," *New York*, vol. 413, 1960.
- [29] T. S. Lammerink, N. R. Tas, M. Elwenspoek, and J. H. Fluitman, "Micro-liquid flow sensor," *Sensors and actuators A: Physical*, vol. 37, pp. 45–50, 1993.
- [30] J. van Tiem, *Modelling, design, fabrication and characterization of a biomimetic angular acceleration sensor*. Msc. presentation, University of Twente, 2014.
- [31] J. Fraden, *Handbook of Modern Sensors*. New York, New York, USA, 2010.
- [32] A. Király and F. Ronkay, "Temperature dependence of electrical properties in conductive polymer composites," *Polymer Testing*, vol. 43, pp. 154–162, 2015.
- [33] E. Ivanov, R. Kotsilkova, H. Xia, Y. Chen, R. K. Donato, K. Donato, A. P. Godoy, R. Di Maio, C. Silvestre, S. Cimmino, *et al.*, "Pla/graphene/mwcnt composites with improved electrical and thermal properties suitable for fdm 3d printing applications," *Applied Sciences*, vol. 9, no. 6, p. 1209, 2019.
- [34] J. Zhang, B. Yang, F. Fu, F. You, X. Dong, and M. Dai, "Resistivity and its anisotropy characterization of 3d-printed acrylonitrile butadiene styrene copolymer (abs)/carbon black (cb) composites," *Applied Sciences*, vol. 7, no. 1, p. 20, 2017.

- [35] M. B. Heaney, "Electrical conductivity and resistivity," *The measurement, instrumentation and sensors handbook*, pp. 1332–1345, 2000.
- [36] L. Brunetti and E. Monticone, "Properties of nickel thin films on polyimide substrata for hf bolometers," *Measurement Science and Technology*, vol. 4, no. 11, p. 1244, 1993.
- [37] D. Nichetti and N. Grizzuti, "Determination of the phase transition behavior of thermoplastic polyurethanes from coupled rheology/dsc measurements," *Polymer Engineering & Science*, vol. 44, no. 8, pp. 1514–1521, 2004.
- [38] D. Magali, "Integrating sensors in components using additive manufacturing," Master's thesis, Hochschule Esslingen, 2016.
- [39] S. Chuayjuljit and S. Ketthongmongkol, "Properties and morphology of injection- and compression-molded thermoplastic polyurethane/polypropylene-graft-maleic anhydride/wollastonite composites," *Journal of Thermoplastic Composite Materials*, vol. 26, no. 7, pp. 923–935, 2013.
- [40] D. Aneli and G. Topchistudies on teshvili, "Conductivity mechanism of electrically conductive polymer compositions," *Int. Polym. Sci. Technol*, vol. 13, pp. 91–2, 1986.
- [41] H. Tang, X. Chen, and Y. Luo, "Studies on the ptc/ntc effect of carbon black filled low density polyethylene composites," *European polymer journal*, vol. 33, no. 8, pp. 1383–1386, 1997.
- [42] C. Klason and J. Kubat, "Anomalous behavior of electrical conductivity and thermal noise in carbon black-containing polymers at tg and tm," *Journal of Applied Polymer Science*, vol. 19, no. 3, pp. 831–845, 1975.
- [43] F. Daniel, N. H. Patoary, A. L. Moore, L. Weiss, and A. D. Radadia, "Temperature-dependent electrical resistance of conductive polylactic acid filament for fused deposition modeling," *The International Journal of Advanced Manufacturing Technology*, vol. 99, no. 5-8, pp. 1215–1224, 2018.
- [44] Z. Instruments, "Principles of lock in detection and state of art." <https://www.proto-pasta.com/pages/conductive-pla>.